Western Barents Sea Circulation and Hydrography, past and present

Eivind H. Kolås[1], Till M. Baumann[1], Ragnheid Skogseth[3], Zoe Koenig[2,1], Ilker Fer[1,3]

[1]Geophysical Institute, University of Bergen and Bjerknes Center for Climate Research, Bergen, Norway
[2]Norwegian Polar Institute, Tromsø, Norway
[3]University Centre at Svalbard, Longyearbyen, Norway

Key Points:

- Circulation pathways and volume transport of Atlantic- and Polar-origin waters in the western Barents Sea are presented.
- Heat exchange across the Barents Sea Polar Front is regulated by the density difference between Polar Water and Atlantic Water.
- Recent Atlantic Water freshening (2018-2022) reduces dense-water production and warm water transport into the basin north of the front.

Corresponding author: Eivind H. Kolås, eivind.kolas@uib.no

Abstract

The Barents Sea is one of the main pathways for warm and saline Atlantic Water (AW) entering the Arctic Ocean. It is an important region for water mass transformation and dense-water production that contribute to the Atlantic meridional overturning circulation. Here, we present data from three cruises and nine glider missions conducted between 2019 and 2022 in the western Barents Sea, and compare with historical data collected from 1950 to 2009. We present circulation pathways, hydrography, heat content and volume fluxes of Atlantic- and Arctic-origin waters. Our observations show that $0.9\pm 0.1\,\mathrm{Sv}$ ($1\,\mathrm{Sv} = 10^6\ \mathrm{m^3\ s^{-1}}$) of Atlantic-origin water reaches the Polar Front (PF) region before splitting into several branches and eventually subducting beneath Polar Water (PW). The observed increased heat content in the AW inflow over the past decades can be traced under the Polar front. The amount of heat stored in the basin north of the PF is determined by the density difference between AW and PW, and reached a maximum in the 90s when PW was particularly fresh. The inflow of Atlantic Water (AW) into the Barents Sea during the period from 2019 to 2022 exhibits a decrease in salinity of up to $0.1\,\mathrm{g\,kg^{-1}}$ compared to previous decades. Consequently, this leads to a reduction in the production of dense water, an increased temperature gradient across the PF, and a reduced poleward transport of warm water.

Plain Language Summary

Warm and salty water from the Atlantic Ocean flows through the Barents Sea on its path towards the Arctic Ocean. It undergoes cooling and freshening due to interactions with the surrounding water and the atmosphere, and eventually encounters much colder and fresher Polar Water, creating a distinct boundary known as the Polar front. We conducted several research missions in the western Barents Sea between 2019 and 2022 and compared the data to historical records collected between 1950 and 2009. The cooled Atlantic Water sinks beneath the Polar Water before continuing towards the Arctic Ocean. In recent decades, the heat content of the Atlantic Water inflow has increased. This additional heat can be traced below the Polar front, leading to an increase in the heat content of the deeper waters north of the front. However, the amount of heat stored north of the front is regulated by the density difference between the Atlantic Water and Polar Water. In the recent period of 2019 to 2022, the Atlantic Water reaching the front has become less salty. As a result, there is a reduced flow of warm water moving northward beneath the Polar Water and a larger temperature difference across the Polar front.

1 Introduction

The Barents Sea is a shallow shelf sea, averaging about 230 m in depth (Figure 1). This sea accounts for about 10% of the Arctic Ocean's surface area and is characterized by ice-free, warmer waters in the south meeting ice-covered, colder waters in the north (Loeng, 1991; Seager et al., 2002; Oziel et al., 2016). The warm water is an extension of the North Atlantic Drift, originating from the Atlantic (Orvik, 2022). In contrast, the cold water in the region originates in the Arctic Ocean through interactions between Arctic waters, sea ice, Atlantic-origin water, melt-water and atmospheric cooling (Timmermans & Marshall, 2020). The marginal ice zone, which marks the transition between these regions, is a vital area for primary production (Reigstad et al., 2002). The Barents Sea supports abundant commercial fish stocks (Johannesen et al., 2012) thanks to its large primary production, making it a critical region in Arctic ecosystems (Reigstad et al., 2002). In addition, the southern Barents Sea is now ice-free year-round due to Atlantification (Årthun et al., 2012; Onarheim & Årthun, 2017). This feature has increased interest in the exploitation of potential oil and gas resources in the shallow sea. To make sustainable decisions for the future in the Barents Sea, a thorough understanding of the ocean circulation and hydrography in the region is necessary.

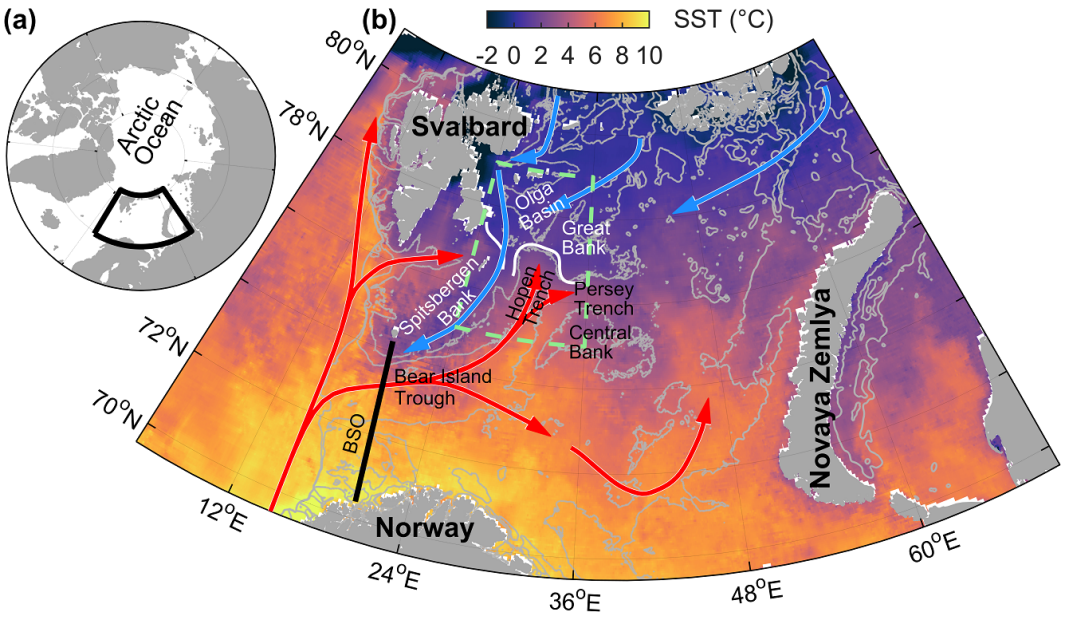

Figure 1. Overview map of the study region. **(a)** The Arctic Ocean where the black box encloses the Barents Sea shown in (b). **(b)** The Barents Sea. Red arrows outline the main Atlantic Water pathways. Blue arrows outline the pathways of Polar water. Black line shows the Barents Sea Opening (BSO). Grey isobaths are drawn at 200, 350 and 500 m depth and are from IBCAOv4. Green dashed box encloses the study region. Sea surface temperature (SST) is from 15 October 2020, and is from the product SEAICE_ARC_SEAICE_L4_NRT_OBSERVATIONS_011_008 at 0.05° resolution based upon observations from the Metop_A AVHRR instrument.

The Norwegian Atlantic Slope Current transports Atlantic Water (AW) along the continental slope west of Norway (Fer et al., 2020; Orvik, 2022). North of Norway, at approximately 72°N, the slope current divides into two branches: one branch continues northward as part of the West Spitsbergen Current, while another branch flows into the Barents Sea via the Barents Sea opening (BSO, Figure 1b). The average annual inflow of AW through the BSO is 2 Sv (1 Sv = 10^6 m^3 s^{-1}), when defined as water with temperatures above 3°C, reaching a maximum of 2.8 Sv in January and a minimum of 1.3 Sv in April (Skagseth et al., 2008; Smedsrud et al., 2010). This AW inflow is the primary source of oceanic heat for the Barents Sea. The observed transport estimates agree well with regional ice–ocean model runs suggesting that the average AW inflow through the BSO is 2.3 ± 0.4 Sv (Årthun et al., 2012). The total average inflow through the BSO, regardless of water mass, is about 3.2 Sv of which 1.2 Sv is thought to recirculate within the Bear Island Trough, making the net inflow through BSO 2 Sv. (Skagseth, 2008; Smedsrud et al., 2010; Loeng et al., 1997).

The AW that flows into the Barents Sea is largely topographically steered in the Bear Island Trough (Loeng, 1991). Once it reaches the Central Bank, the inflowing AW splits into two branches: one that continues eastward south of the Central Bank, and another that moves northward along the Hopen Trench (Loeng, 1991; Årthun et al., 2012; Oziel et al., 2016). The branch south of the Central Bank occupies the southern half of the Barents Sea (Oziel et al., 2016; Barton et al., 2018). Yet, the partitioning of the AW transported eastward south of the Central Bank and northward into the Hopen Trench is unknown because transport estimates are lacking. The Hopen Trench branch continues northward toward the Great Bank, where it again bifurcates: one branch flows eastward into the Persey Trench, and the other continues up the Hopen Trench (Loeng, 1991). The details of these branches, including their volume transport, heat content, pathways, and modification as they reach the northern Barents Sea, are not well documented.

The northwestern Barents Sea is occupied by Polar Water (PW, $\Theta < 0$°C and $\sigma_0 <$ 1027.97 kg m^{-3}), which enters the Barents Sea from the north (Loeng, 1991; Lien et al., 2017). The oceanographic front where PW meets AW is named the Barents Sea Polar Front (PF) (Loeng, 1991; Våge et al., 2014; Oziel et al., 2016). The PF is an important site for water mass transformation and has significant implications for local biogeochemistry and biology, as well as the overturning circulation and ventilation of the Arctic Ocean (Årthun et al., 2011; Våge et al., 2014). The location of the PF has been remarkably stable in the western Barents Sea, following the 200-250 m isobath along the southern slope of the Spitsbergen Bank to the Great Bank (Johannessen & Foster, 1978; Gawarkiewicz & Plueddemann, 1995; Oziel et al., 2016). However, due to sparse data coverage, our current understanding of the circulation of AW south of the PF and the intricate patterns of circulation and mixing within the PF remains limited.

Studies on the southeastern slope of the Spitsbergen Bank have reported conflicting findings on the direction of the flow of AW. While some studies indicate that a warm-core jet of AW flows northeastward along the 300 m isobath (Loeng, 1991; Li & McClimans, 1998), others have observed a westward flow of AW on the southern slope of the Spitsbergen Bank, between the 260 and 400 m isobaths (Parsons et al., 1996; Gawarkiewicz & Plueddemann, 1995). The westward flow of AW is attributed to recirculating AW within the Bear Island Trough (Skagseth, 2008). Further observations suggest that northeast of the recirculating branch, AW flows clockwise around the Hopen Trench due to potential vorticity constraints in a basin with a shallower northern outflow depth than inflow (Barton et al., 2018). However, the circulation south of the Polar Front (PF) in the Barents Sea is complex and influenced by various factors, including sea level, tidal flows, and winds, which change the dynamics of the front (Fer & Drinkwater, 2014; Våge et al., 2014). In addition, the position of the front on the southern slopes of the Spitsbergen Bank is affected by the climate of the Barents Sea, with the front shifting upslope in warmer periods with stronger winds from the south compared to colder periods (Ingvaldsen, 2005).

These findings have important implications for the future PF as the Barents Sea transitions towards conditions where the inflowing AW is warmer and volume flux is larger (Skagseth et al., 2020).

Time series of AW inflow through the BSO show that the temperature of the AW core increased by 1°C between 1965 and 2006, and the volume flux increased by 0.1 Sv per year between 1997 and 2006 (Skagseth et al., 2008). These observations are in agreement with more recent studies showing that the AW volume fraction in the Barents Sea has increased from about 10% in 1980 to about 30% in 2011 (Oziel et al., 2016). This so-called "Atlantification" has led to increased production and northward expansion of boreal species (Ingvaldsen et al., 2021), and has been strongly correlated with the retreat of the sea ice edge (Årthun et al., 2012). The sea ice area in the Barents Sea was reduced by 50% between 1998 and 2008, and the sea ice concentration over the ice-covered zone in the Barents Sea has decreased by almost 7% per decade from 1982 through 2020 (Årthun et al., 2012; Mohamed et al., 2022). However, the position of the PF in the western Barents Sea appears to be unaffected by the sea ice edge and has remained relatively stable, despite an observed increase in the sea surface temperature gradient associated with the PF. (Barton et al., 2018).

The purpose of this paper is to provide a detailed account of the circulation and hydrography of AW in the western Barents Sea within the region enclosed in Figure 1b. Specifically, we concentrate on the area where the warm AW and cold PW converge, maintaining the PF. We present recent observations and compare them to historical data collected in the same region. This area is of particular interest due to the limited knowledge of the route taken by the AW flowing northward towards the PF and the modification the AW undergoes along this route.

2 Data

Detailed ocean hydrography and current observations were collected from 2018 to 2021, focusing on the northwestern Barents Sea (Figure 1b). This comprehensive dataset includes measurements from three scientific cruises and nine ocean glider missions. In order to enhance our understanding of the Barents Sea circulation, we also incorporated shipboard acoustic Doppler current profiler data from five additional cruises spanning the same period. All of these data were obtained as part of the Nansen Legacy project. For convenience, we refer to this dataset as the "recent data" or the "Nansen Legacy data." The recent data primarily cover the fall and winter seasons, specifically from August to February. In addition, we present historical data from the UNIS hydrographic database, consistently using the conductivity-temperature-depth (CTD) profiles collected between August and February. Further information about the platforms used is given in the subsequent subsections. An illustration of data coverage and data tracks is provided in Figure 2. Detailed metadata for the cruises and glider missions are listed in Table 1.

2.1 Hydrographic Measurements From the Nansen Legacy Cruises

The cruises were conducted on board the Research Vessels (RV) G.O. SARS between 6 and 27 October 2020 (Fer et al., 2021), Kronprins Haakon between 9 February and 1 March 2021 (Nilsen et al., 2021), and Kristine Bonnevie between 28 September and 13 October 2022 (Baumann et al., 2023). CTD profiles during all cruises were collected using a Sea-Bird Scientific, SBE 911plus system. The CTD salinity was calibrated using water samples taken at all stations at the deepest profile depth. In total, 64, 89, and 62 CTD profiles were collected during the cruises, respectively. CTD profiles, together with the current profiles (Section 2.2), of the October 2020 cruise are available

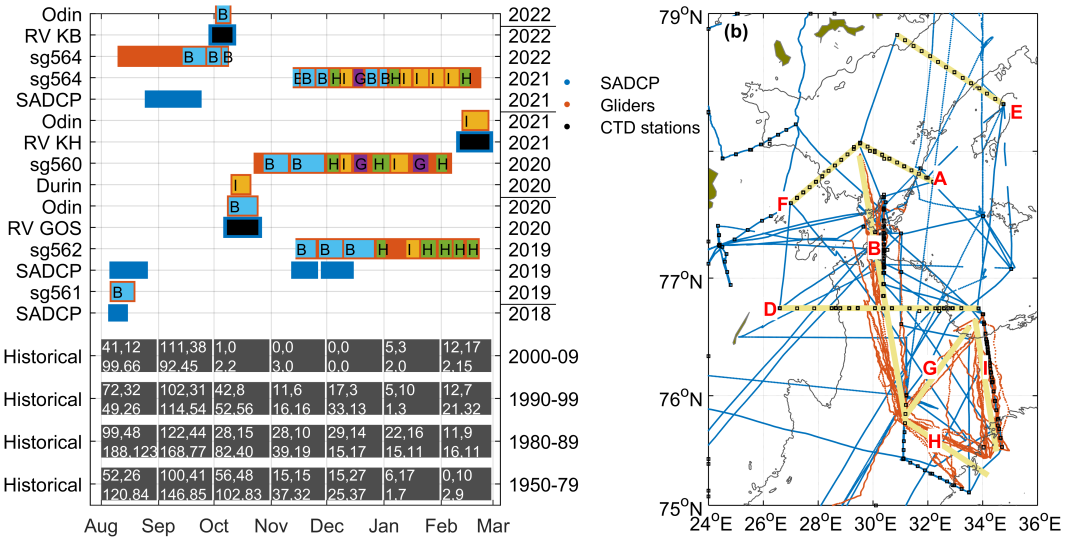

Figure 2. **(a)** Coverage of the different data presented in this study. The mission span of gliders is marked with orange fill and the mission tracks are shown in (b) using the same color. Selected sections in all missions are indicated by section names and a color code to highlight the temporal coverage and repetitions of the sections. The target position of the sections is shown in (b). Duration of cruises with SADCP data is indicated using blue fill in (a) and cruise tracks with the same color in (b). The specific cruises with hydrographic measurements are identified with the vessel names (RV KB: Kristine Bonnevie, RV KH: Kronprins Haakon, and RV GOS: G.O. Sars) and the black fill indicates CTD sampling, with stations marked with the same color in (b). The number of historical CTD profiles included in Sections B, H (upper two numbers), and D and I (lower two numbers) are listed for the individual months and decades. **(b)** Position of the different data collected. Grey line shows the 200 m isobath. Yellow lines indicate our predefined sections with the corresponding names (red letters).

Table 1. Glider and cruise metadata. Sections refer to the sections names listed in Figure 2b. The number of CTD profiles from the cruises is the sum of shipboard CTD and MSS profiles. Offsets applied to cruise CTD is that for the MSS.

Vessel	**Start/ end**	**Sections**	**# of CTD profiles**	**Offset applied to salinity / temperature**
sg561	7 August 2019/ 19 August 2019	B	308	0.016 / 0.082°C
sg562	15 November 2019/ 1 March 2020	B, H, I	2,568	−0.005 / −0.060°C
RV GOS	6 October 2020 27 October 2020	B, H, I, D, F, A, E	269	−0.018 / N/A
Odin	8 October 2020/ 24 October 2020	Polar Front	800	0.014 / 0.054°C
Durin	10 October 2020/ 20 October 2020	I	678	N/A
sg560	22 October 2020/ 11 February 2021	B, H, I, G	2,534	0.017 / −0.209°C
RV KH	9 February 2021 1 March 2021	B, I	261	−0.018 / N/A
Odin	12 February 2021/ 25 February 2021	I	748	0.0045 / 0.05°C
sg564	12 November 2021/ 22 February 2022	B, H, I, G	3,426	0.015 / 0.02°C
sg564	9 August 2022/ 9 October 2022	B	2,492	0.015 / 0.02°C
RV KB	28 September 2022 13 October 2022	D, I, B F, A	328	N/A
Odin	2 October 2022/ 9 October 2022	Polar Front	402	N/A

from (Fer, Baumann, Hana, et al., 2023)[1]. Pressure, temperature, and practical salinity data are accurate to ±0.5 dbar, $\pm 2 \times 10^{-3}$ °C, and $\pm 3 \times 10^{-3}$, respectively. CTD data were processed using the standard SBE Data Processing software.

In addition to the shipboard SBE CTD system, profiles were collected using a Microstructure Sensor Profiler (MSS90L, Sea&Sun Technology, Germany, MSS hereafter). MSS is a loosely-tethered free-fall instrument equipped with turbulence sensors (not reported here) and conventional CTD sensors for precision measurements. CTD profiles from the MSS enhanced the hydrographic measurements from the cruises. The CTD profiles from the MSS have been corrected against the ship CTD during post-processing, by applying offsets when applicable. The largest salinity offset applied was 0.018 (Table 1). A total of 205, 172 and 266 profiles were collected using the MSS during the three cruises, respectively, which can be obtained from Fer, Baumann, Kalhagen, et al. (2023); Fer, Skogseth, et al. (2023); Fer, Baumann, Elliot, and Kolås (2023).

Conservative Temperature, Θ, and Absolute Salinity, S_A, were calculated using the thermodynamic equation of seawater (IOC et al., 2010), and the Gibbs SeaWater Oceanographic Toolbox (McDougall & Barker, 2011).

2.2 Current Profiles From Cruises

Current profiles were obtained using acoustic Doppler current profilers (ADCPs) in two different configurations: ship-mounted ADCP (SADCP) for continuous measurements and ADCP systems integrated into the CTD frames (lowered-ADCP, LADCP) for station-based measurements. The CTD frames on all vessels were equipped with a pair of 300 kHz Teledyne RD Instruments (RDI) Sentinel Workhorses, with one mounted pointing downward and the other upward. The LADCPs were synchronized and configured to provide vertically averaged data in 8 m bins. Compasses were calibrated, resulting in errors less than 5°. LADCP data were processed using the LDEO software version IX-13 of Visbeck (2002). The LADCP profiles were constrained using navigation data and the current profiles from the SADCPs.

All research vessels had Teledyne RDI Ocean Surveyor SADCPs operating at one or two acoustic frequencies. In this study we use the current profiles collected by the 150 kHz SADCP from RV Kronprins Haakon and RV Kristine Bonnevie. The SADCPs on Kronprins Haakon were flush-mounted in the hull for protection when moving through ice. From RV G. O. SARS we use the 75 kHz SADCP. The 150 kHz SADCPs collected profiles in 4 m bins using narrowband mode for optimal range, while the 75 kHz SADCP measured in 8 m bins. SADCP data were collected using the onboard VmDAS software or the University of Hawaii data acquisition software, depending on the vessel. Post-processing was done using the University of Hawaii CODAS software, to an uncertainty of 2–3 $\mathrm{cm\,s^{-1}}$ (Firing & Ranada, 1995).

In addition to the current measurements obtained during the cruises described in this study, we also incorporate SADCP data from 5 additional cruises conducted in the region during the fall and winter seasons (August to February) between 2018 and 2020. For more detailed information regarding the SADCP data obtained from these other cruises, the reader is referred to Cannaby et al. (2022).

2.3 Ocean Glider Data

An ocean glider (glider hereafter) is a buoyancy-driven, remotely-piloted underwater vehicle. Five Kongsberg Seaglider missions and four Teledyne G3 Slocum glider mis-

[1] a note to the editor and reviewers: the data from the other two cruises are prepared and will be submitted during the review process

sions were conducted in the Barents Sea in the period from 2019 to 2022 (E. Kolås, 2022). Details about the individual missions are shown in Table 1. The main objective was to map the distribution and circulation of the AW in the region (Figure 1), and to collect detailed observations on the interaction between the AW and PW along the Polar Front between the Spitsbergen Bank and Great Bank. The glider tracks are shown in Figure 2b, and the sections sampled by the individual gliders are listed in Table 1 as well as shown in Figure 2a. A total of 13,956 profiles were collected and analyzed. The typical horizontal distance between subsequent surfacing locations was 1 km. The gliders operated between the surface and 0-20 m above the seafloor, sampling CTD on both dives and climbs. For each dive, a depth-averaged current (DAC) was estimated based on the deviation between the actual surfacing location and the expected surfacing location from a hydrodynamic glider flight model. Absolute geostrophic currents are calculated from glider hydrography and DAC as described in section 3.2. During post-processing, each profile was despiked by removing values exceeding twice the root mean square (rms) of the five surrounding values. In addition, outliers exceeding three standard deviations over all profiles at each pressure level were removed.

2.3.1 Seagliders

Each of the Seagliders were equipped with a Paine strain-gauge pressure sensor, a SBE CT Sail and an Aanderaa dissolved oxygen sensor. The Seagliders operated with a vertical velocity close to $8\,\mathrm{cm\,s^{-1}}$, and sampling rates normally aimed to sample conductivity and temperature every meter while oxygen was sampled every 5 m. The Seaglider data sets were processed using the University of East Anglia Seaglider toolbox (`http://www.byqueste.com/toolbox.html`), based on the methods described by Garau et al. (2011); Frajka-Williams et al. (2011). Manual flagging was applied to the salinity and temperature profiles during processing. Processed S_A and Θ are accurate to $0.01\,\mathrm{g\,kg^{-1}}$ and 0.001°C, respectively, and DAC is accurate to $0.01\,\mathrm{m\,s^{-1}}$ (*Seaglider Quality Control Manual*, 2012, p. 9). Post-processing revealed noisy data with overturns, typically through the pycnocline and the apogee of the dive, but also randomly throughout profiles. The noisy data is likely due to the Conductivity-Temperature sensor being unpumped. When the flow past the sensor changes due to a change in pitch or vertical velocity, the salinity estimates can be erroneous due to a misalignment of conductivity and temperature. Because of the uncertainty in the salinity estimates, we removed instabilities where the absolute difference between the density profile and the sorted-density profile was larger than $0.02\,\mathrm{kg\,m^{-3}}$. The number of data points removed was less than 1 % of the total data, and overall does not affect the averaged and objectively mapped fields used in our analysis. Finally, salinity and temperature offset corrections were applied after comparing the deep part of Seaglider dives to nearby CTD profiles collected from research vessels typically within 3 days and 5 km from the Glider profile. The offsets applied to the different missions are listed in Table 1.

The gliders in the Barents Sea were operated with an ice-avoidance algorithm in order to prevent losing the instrument in the ice. This algorithm uses acoustics to detect ice keels in addition to temperature measurements to identify freezing temperatures near the surface. If sea ice or near freezing-point temperatures were detected, a new dive would start without surfacing. On several occasions, northerly winds pushed sea ice over the gliders, preventing them from surfacing and obtaining a GPS fix. These events normally lasted for only a few dives, yet on a few occasions the glider was under ice for longer than 24 hours, causing the glider to turn to a predefined point and head away from the ice (so-called "escape mode"). The longest stretch without a GPS fix lasted for 34 dives or about 44 hours. In such situations without a GPS fix, DAC cannot be estimated. For each dive conducted without a GPS fix, longitude and latitude coordinates along the dive tracks were linearly interpolated between the two available GPS fixes, assuming the glider continued in a straight line. In the few cases when the glider turned south in the escape mode while under sea ice, the northernmost position was extrapolated based on the most

recent horizontal velocity estimate, the compass heading, and the depth of the seabed. More details on the processing and glider deployments are given in E. Kolås (2022).

2.3.2 Slocum gliders

Two electric 1000-m G3 Slocum gliders, Odin and Durin, were used during the October 2020 cruise, while only Odin was used during the February 2021 and October 2022 cruises (Table 1). Both gliders carried a pumped SBE CTD sensor (CTD41CP). The glider sampled at 0.25 Hz with a typical vertical velocity of $15\,\mathrm{cm\,s^{-1}}$. The glider was configured to inflect 15 m above the seabed. Data were processed using the quality control procedures from the Balearic Islands Coastal Observing and Forecasting System (SOCIB) data processing toolbox (Troupin et al., 2015). Final profiles have a horizontal along-track spacing of about 0.5 km and 1 m vertical spacing. Odin additionally carried a turbulence package for measuring small-scale shear across the Polar Front. The turbulence data set is part of a different study and is not further described here.

2.4 Historical data

Historical composite sections of Conservative Temperature and Absolute Salinity over the periods 1950-79, 1980-89, 1990-99, and 2000-09 were made from hydrographical profiles extracted from the UNIS hydrographic database (UNIS HD; (Skogseth et al., 2019)). This data set is a collection of temperature and salinity profiles from the area 0-34°E and 75-83°N. Duplicate data and outliers have been removed before the analysis. In this study we only considered CTD profiles collected between August and February, and a total of 3,916 profiles were included. Note that UNIS HD also consists of data extracted from other data publishers. For details on the main data contributors to UNIS HD, the reader is referred to Skogseth et al. (2019).

3 Methods

3.1 Water masses

The water masses used in this study are listed in Table 2, and follow Sundfjord et al. (2020). These definitions are based on previous water mass definitions in literature such as Lind et al. (2018); Loeng (1991); Rudels et al. (2005). However, we have made a modification to the definition of warm Polar Water (wPW), by including only waters with potential density anomaly $\sigma_0 > 27.8$. The reason for this is that we only consider the wPW which is a mixture between AW and PW, excluding surface waters influenced to a greater extent by seasonal processes such as atmospheric heating and ice melting.

3.2 Objective interpolation of depth average currents

In this study, a total of 59,000 SADCP profiles, 198 LADCP profiles and 7,195 DAC estimates from glider dives have been used. We removed the barotropic tidal currents from the SADCP and LADCP profiles using the 2018 version of the Arctic Ocean Inverse Tidal Model on a 5 km grid (Arc5km2018) (Padman & Erofeeva, 2004). LADCP profiles were vertically averaged over the whole water column, whereas for the SADCP profiles, the upper 16 m were removed before averaging (16 m was the largest blanking distance used on the different SADCPs). Depth-averaged SADCP profiles were subsequently bin-averaged in 10 km by 10 km horizontal bins.

A typical glider dive in the Barents Sea lasted for about an hour and covered about 1 km horizontal distance. To remove the barotropic tide from DAC, we interpolated the DAC time series to hourly data and used a 24 h low pass filter. The detided DAC were then averaged over 6 hour bins. A final 10 km by 10 km bin-averaging was applied to com-

Table 2. Water mass definitions following Sundfjord et al. (2020), using Conservative Temperature, Θ, Absolute Salinity, S_A, and potential density anomaly, σ_0. Note that our definition of the warm Polar Water (wPW), includes only waters with $\sigma_0 > 27.8$ in order to exclude surface waters from the wPW. Instead, we name the wPW with $\sigma_0 < 27.8$ Surface Water (SW).

Water mass	Θ **(°C)**	S_A **(g kg^{-1})**	Density ($\rho - 1000\,\mathrm{kg\,m^{-3}}$)
Atlantic Water (AW)	$\Theta \geq 2$	$S_A \geq 35.06$	
Polar Water (PW)	$\Theta < 0$		$\sigma_0 < 27.97$
warm Polar Water (wPW)	$\Theta \geq 0$	$S_A < 35.06$	$\sigma_0 \geq 27.8$
Surface Water (SW)	$\Theta \geq 0$	$S_A < 35.06$	$\sigma_0 < 27.8$
modified Atlantic Water (mAW)	$0 \leq \Theta < 2$	$S_A \geq 35.06$	
Intermediate Water (IW)	$-1.1 \leq \Theta < 0$		$\sigma_0 \geq 27.97$
cold Barents Sea Dense Water	$\Theta < -1.1$		$\sigma_0 \geq 27.97$

bine the detided and averaged SADCP, LADCP and glider DAC before objective interpolation.

Care must be taken to avoid unrealistic diverging or converging flows in the objectively interpolated fields of ocean currents. Here we have constrained the interpolated fields to be divergence-free. In objective interpolation, we used a horizontal correlation length scale of 50 km, obtained from a variogram analysis of the depth average currents after final bin-averaging. Variogram analysis calculates the variance in the difference between data points as a function of the distance between the data points. The correlation length scale is then set at the distance where the variance ceases to increase. More details on variogram analysis are given in the appendix of E. H. Kolås et al. (2020). We objectively interpolated onto a horizontal grid with 10 km resolution. Mapped currents for which the relative error exceeded 40% of the absolute current were removed. We also removed currents mapped at locations where the water depth was shallower than 50 m. The 50 m depth criterion was set as we have few measurements in the shallow regions where the tidal currents are relatively large.

3.3 Composite sections

In order to remove fine-scale variability and obtain fields representative of the average hydrography and geostrophic currents, we produce composite sections. The composite sections are along the predefined transects marked by yellow lines in Figure 2b, along which we have focused our data sampling. The horizontal grid spacing along each section was set to 1 km. For every data point (all Θ and S_A profiles, and SADCP and glider DAC), an incrementally increasing search radius of 5, 10, 20 and 30 km was used to look for predefined grid points along the target section. When two or more grid points were within the search radius of a data point, the data point was moved along isobaths onto the section, thus assuming topographic steering. The bottom depth along the section, as well as for the data points, was determined using IBCAO-v4. If by chance two or more locations on the predefined section (within the search radius of the data point) had the same bottom depth, the location nearest to the data point was chosen. Finally, Θ and S_A profiles along the section were bin-averaged over 5 km horizontal and 10 m vertical bins before objectively mapping onto a 1 km by 5 m grid (horizontal by vertical). Historical CTD profiles were averaged over 5 km horizontal and 20 m vertical bins before objectively mapping onto a 1 km by 5 m grid. To obtain absolute geostrophic velocities along the composite sections, we need reference depth-averaged velocities averaged and smoothed with consistent time and length scales. Depth average SADCP and

glider DAC were bin-averaged over 5 km horizontal bins and linearly interpolated onto the 1 km resolution of the target section, and smoothed using a 15 km moving average.

When objectively mapping the composite sections, correlation length of 30 km and 50 m were used as horizontal and vertical scales, respectively, determined from the variogram analysis as described in section 3.2. To remove unrealistic values caused by interpolation, temperatures below freezing were set to the freezing point, and values below the seabed were removed. In addition, mapped values for which the relative error (the absolute error divided by the data value) exceeded 5% were removed. The low threshold of 5% was used due to the high resolution of data points compared to the long correlation length. That is, we have binned observations for every 5 km along the section while using a 30 km correlation length scale, resulting in small objective mapping error.

We produced geostrophic velocity fields using the objectively mapped Θ and S_A sections from the cruises and gliders, and the historical section across the PF (Section B). To avoid spurious unstable layers arising from the combination of the independently mapped fields, we calculated density and reproduced the S_A fields using sorted (by stability) and smoothed density. Density was smoothed over 2 km horizontal and 10 m vertical distance (2 by 2 grid points). Absolute geostrophic velocity, u_g, was obtained by removing the depth average relative geostrophic velocity and adding gridded observed SADCP and glider DAC.

As we estimate mean properties and volume transports from objectively mapped fields of Θ, S_A and u_g, the uncertainty in our measurements is essential. While the instrument error of the many individual instruments is small, the instrument calibration error may not be. Here we cross calibrate several different instruments by comparing nearby CTD profiles from gliders and MSS to ship CTD profiles and applying an appropriate offset. We trust the ship CTD to be accurate and the profiles we compare are usually less than 5 km and 3 days apart, however the region is highly dynamical and the comparison may be inaccurate. We argue that our Θ and S_A uncertainty is at a similar magnitude as the offsets we typically apply. That is $0.02\,\mathrm{g\,kg^{-1}}$ and 0.1°C for S_A and Θ, respectively, rounded to the first significant digit (Table 1).

Volume transport estimates for individual water masses are calculated from the u_g fields. These estimates are most sensitive to the water mass boundaries and the 2-3 $\mathrm{cm\,s^{-1}}$ SADCP uncertainty. Here we estimate the error by applying an upper and lower bound on the area corresponding to the S_A and Θ uncertainty. Then we add one thousand Gaussian distributed random error matrices where the error range from -3 to $3\,\mathrm{cm\,s^{-1}}$ corresponding to the SADCP uncertainty. Errors are the root-mean-square of the difference between calculations from the original gridded field and each of the upper and lower boundary. The resulting volume transport error is always less than 0.1 Sv, and typically around 0.05 Sv.

3.4 Heat and salt content

Heat content per volume, HC, is calculated for all composite sections below 50 m depth, and is presented as average heat content per volume $\overline{\mathrm{HC}}$. We calculate heat content for the Atlantic Water domain ($\Theta \geq 0.1$°C) and Polar Water domain ($\Theta < 0.1$°C) separately. The 0.1°C boundary is the isotherm defining the PF as described in Section 3.6. For each composite section we calculate heat content as

$$\overline{\mathrm{HC}} = \frac{\int_A C_p \rho_0 \Theta \, dA}{A}, \tag{1}$$

where $C_p = 3992\,\mathrm{J\,kg^{-1}\,K^{-1}}$ is the specific heat capacity of water for use with Θ (McDougall & Barker, 2011), ρ_0 is the potential density and A denotes the area.

Heat content is also calculated for horizontally interpolated layers in a similar manner. For each profile we calculate the layer averaged heat content per volume as

$$\overline{\mathrm{HC}} = \frac{\int_{z_1}^{z_2} C_p \rho_0 \Theta \, dz}{z_2 - z_1}, \tag{2}$$

where z_1 and z_2 are the depth limits for the range we integrate over. Similarly, layer averaged salt content per volume is calculated as

$$\overline{\mathrm{SC}} = \frac{\int_{z_1}^{z_2} \rho_0 S_A \, dz}{z_2 - z_1}. \tag{3}$$

$\overline{\mathrm{HC}}$ and $\overline{\mathrm{SC}}$ are then objectively interpolated as described in Section 3.5. Uncertainties in $\overline{\mathrm{HC}}$ and $\overline{\mathrm{SC}}$ are calculated using the upper and lower bound of Θ and S_A as described in Section 3.3.

3.5 Objectively interpolated horizontal layers

Objectively mapped horizontal fields of Θ, S_A, $\overline{\mathrm{HC}}$ and $\overline{\mathrm{SC}}$, for different depth-layers and different time periods were produced using the recent and historical CTD profiles. Individual profiles were vertically averaged over the desired layer depth, before bin-averaging over 10 km by 10 km horizontal bins. To ensure that the vertically averaged values were representative of the layer, thresholds were set on the minimum amount of data points averaged, and the average depth of the data points compared to the middle depth of the layer. For the 50-100 m layer, a minimum of 5 data points whose mean depth were within 15 m of the middle depth of the layer were required. Horizontal correlation length scales were set to 60 km and final gridded product had a 2 km resolution.

3.6 Barents Sea Polar Front position

The position of the PF is determined following the method described by Oziel et al. (2016). Oziel et al. (2016) calculated two different fronts, a northern and a southern front based on the temperature and salinity fields, respectively. In our study, we focus only on the position of the northern front obtained from the temperature field. To achieve this, we create a horizontally mapped field by combining all available temperature (Θ) data for the 50-100 m layer, including both historical and recent data, using the method described in Section 3.5. Subsequently, we calculate the absolute temperature gradients across this field. We then construct a histogram with 0.05°C bins of the Θ values where the temperature gradient exceeds $0.06\,^{\circ}\mathrm{C\,km^{-1}}$. The PF is then defined as the isotherm corresponding to the modal value of the histogram, here equal to the 0.1°C isotherm, with one standard deviation of 0.4°C. While the modal value is somewhat sensitive to the lower temperature gradient limit, the position of the front along Section B varies less than 15 km, within ±1 standard deviation.

4 Results

The AW inflow into the Barents Sea is a topographically steered current, following the eastern boundary of the Bear Island Trough. Here we describe the evolution of the AW from the northeasternmost part of the Bear Island Trough where it splits into the two paths toward the Hopen Trench and the Persey Trench, and the continuation across the PF into the Olga Basin (Figure 1b). We first present the recent Nansen Legacy observations (2019-2022), followed by the historical data dating back to 1950.

4.1 Hydrography and circulation south of the PF from recent observations (2019-2022)

Section H, located on the northwestern slope of the Central Bank, is filled with AW at isobaths deeper than 200 m and 50-100 m above the seafloor (Figure 3, Sec H). The

Table 3. Volume transport, V_{u_g} (Sv), for the different water mass definitions, through the different composite sections. All transport estimates are calculated from the u_g fields in Figure 4a and rounded to the nearest decimal. Transport estimates are divided into positive and negative transport estimates, corresponding to positive or negative u_g, where negative transport estimates are given in parentheses. Volume transport errors are as described in Section 3.3 are always less than 0.1 Sv, and typically around 0.05 Sv.

Sec.	AW	mAW	wPW	PW	Total V_{u_g}
H	0.6	0.3	0.1	n/a	0.9
I	0.0	0.3 (-0.1)	0.2	0.0	0.5 (-0.2)
G	0.2	0.1	0.2	0.0	0.5
D	0.2	0.3	0.1	0.1 (-0.1)	0.9 (-0.3)
B(PF)	n/a	n/a	0.1	0.2	0.3
A	n/a	0.1	0.2	0.2	0.5
F	n/a	n/a	0.1	0.1 (-0.3)	0.1 (-0.5)
E	n/a	n/a	0.1	0.3 (-0.3)	0.5 (-0.3)

geostrophic current, u_g, distribution suggests two dynamical cores (Figure 4). One branch is located on the upper slope above the 300 m isobath, and one on the lower slope towards the center of the trough. This bifurcation is likely a result of diverging bathymetry south of Section H, and is also seen in the depth-averaged currents (Figure 4b).

The volume transport through Section H is 0.9 Sv, divided equally among the upper and lower branches. Of this, 0.6 Sv is identified as AW (Table 3). The mean temperature of the inflowing AW in the upper branch is 2.4°C, 0.2°C less than in the lower branch, indicating that the AW closer to the center of the trough is relatively less cooled compared to the upper slope. The mean salinity is 35.11 g kg^{-1} for both branches.

The AW at Section H is surrounded by modified AW (mAW) and warm Polar Water (wPW) on the shallow bank and at depth, for which the volume transport estimates are 0.3 and 0.1 Sv, respectively (Figure 5a). Modified AW here is the AW cooled below 2°C, while the wPW is a mixture of AW and PW (see water mass definitions in Table 2 and in the $\Theta - S_A$ diagram in Figure 5a). The AW reaching the northern part of the Bear Island Trough is transformed mainly through cooling by the atmosphere, hence the relatively small amount of wPW (Figure 5a and b). Continuing from Section H, the inflow splits into two branches, one continuing east through the Persey Trench and one continuing north up the Hopen Trench (Figure 4b).

Section I completely covers the eastward propagating water masses through the Persey Trench. The AW core subducts from Section H to I, forming a subsurface Θ maximum core located on the southern slope between the 300 m and 200 m isobaths (Figure 3a, Sec I). The u_g core of the eastward propagating current is located closer to the center of the trench than the AW core, with westward flowing currents to the north and weak eastward flowing currents to the south (Figure 4a). While the eastward AW transport through Section I is negligible, the eastward transport of mAW and wPW is 0.3 and 0.2 Sv, respectively, resulting in a total eastward transport of 0.5 Sv. On the northern slope, a surface-intensified current directed westward entrains mAW, resulting in a westward transport of mAW of 0.1 Sv. Westward flowing transport estimates are listed in Table 3; note, however, that the currents at the section edges may not be fully captured.

Sections B, G, and D mainly cover the northward propagating water masses along the Hopen Trench towards the sill that separates the Atlantic domain from the Polar domain in the Olga Basin. Absolute geostrophic velocities, u_g, through Section G are mainly

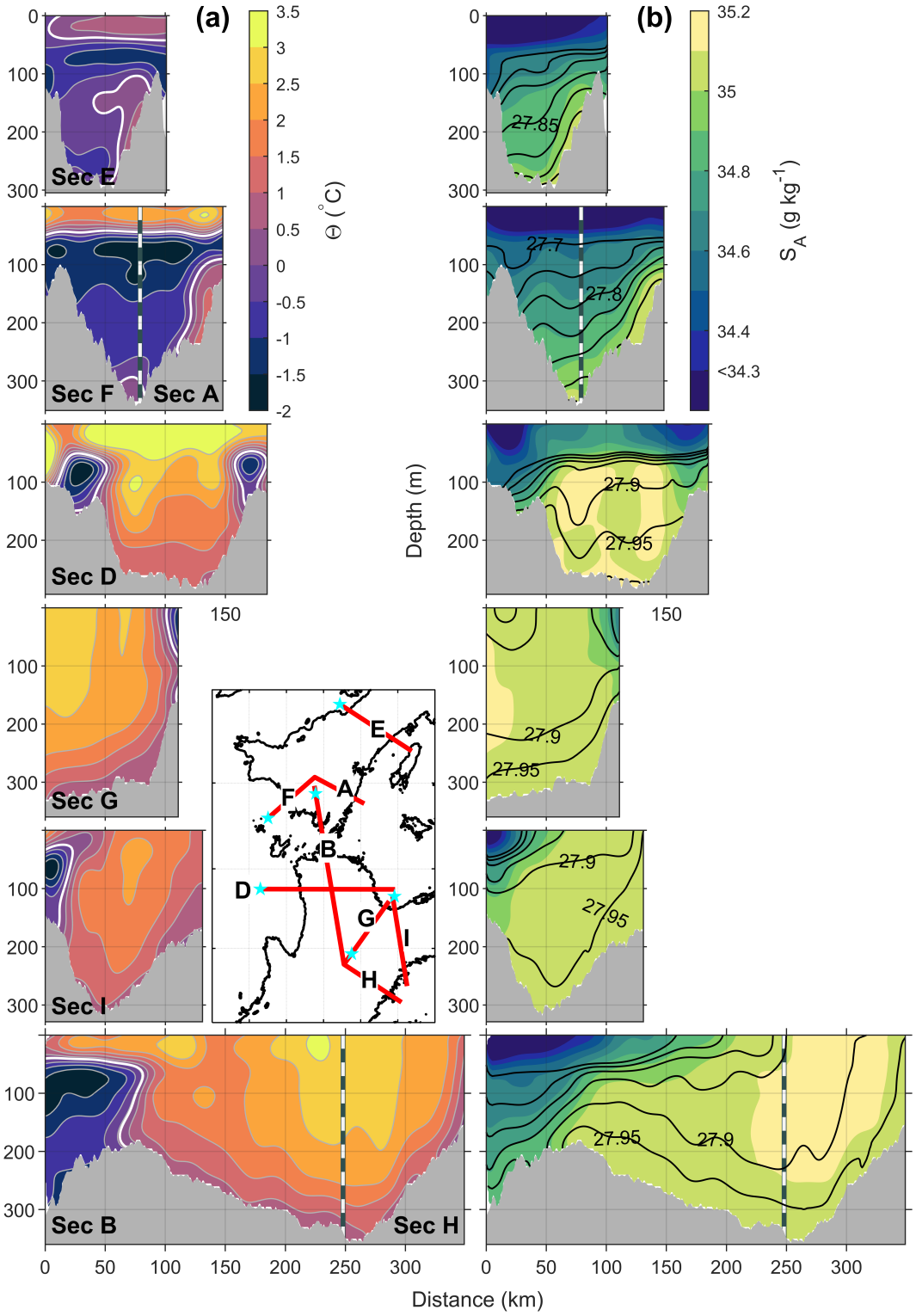

Figure 3. Hydrographic cross-sections of **(a)** Conservative Temperature, Θ, and **(b)** Absolute Salinity, S_A, along the sections defined in Figure 1b, also indicated on the map here. Horizontal distance is referenced to the edge of the section, marked by blue stars on the map. Sections F-A and B-H are joined at the location marked by the vertical bars. White line in (a) is the 0.1°C isotherm. Black contours in (b) show isopycnals at every 0.05 kg m^{-3} interval, starting at 27.7 kg m^{-3}. Analysis period covers the months from August to February between 2019 and 2022 (see Figure 2a).

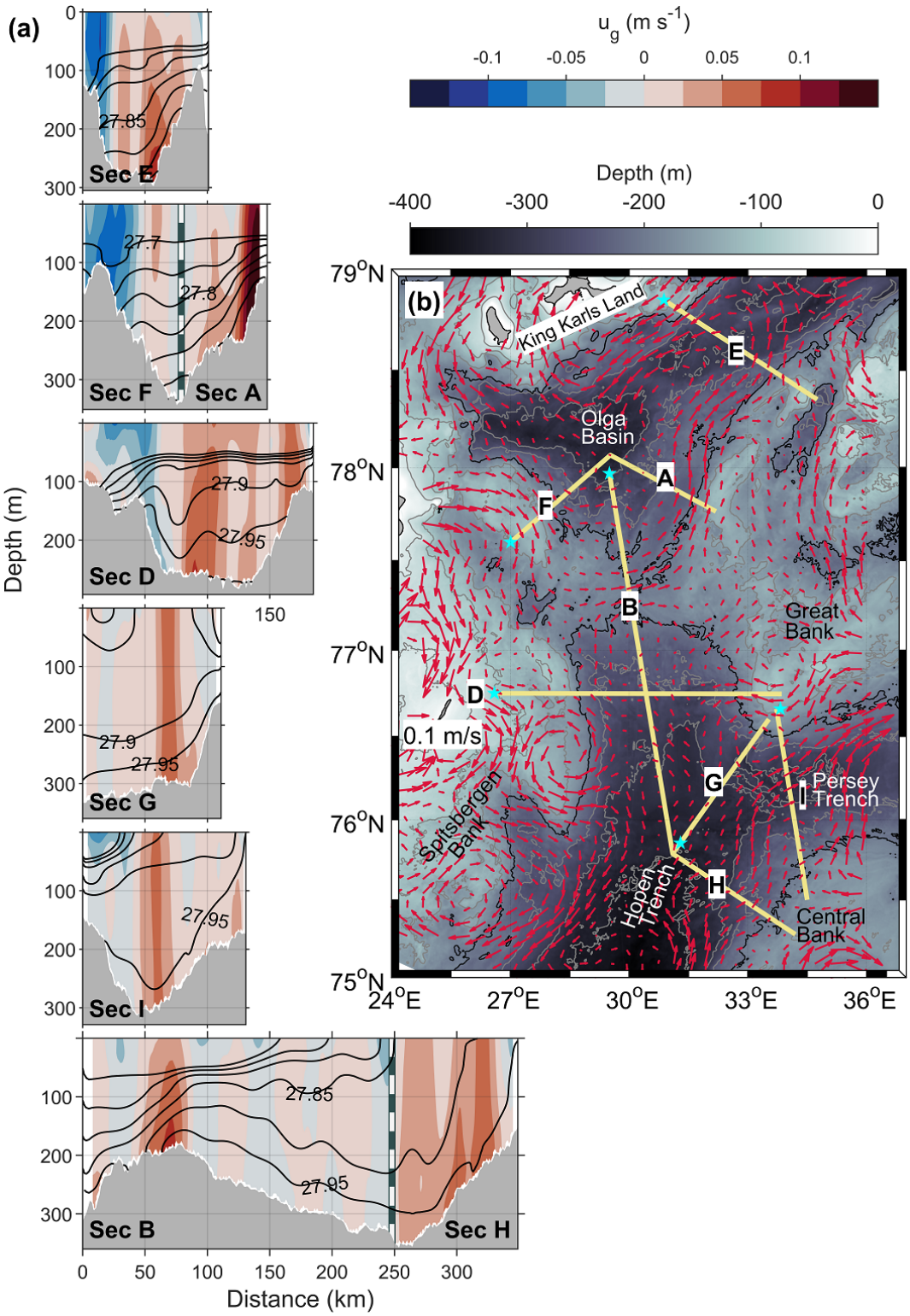

Figure 4. **(a)** Absolute geostrophic velocities, u_g, normal to the sections marked in (b). 0 km is the edge of the section as marked by the blue star in (b). Positive velocities are directed into the page, downstream of the viewer. Black contours in (a) show isopycnals at every 0.05 kg m^{-3} interval, starting at 27.7 kg m^{-3}. **(b)** Objectively mapped, divergence-free, depth-averaged currents from SADCP, LADCP and glider DAC. Gray lines are isobaths drawn at every 50 m from 50 to 300 m depth. Black line is the 200 m isobath. Data included covers the months from August to February between 2018 and 2022.

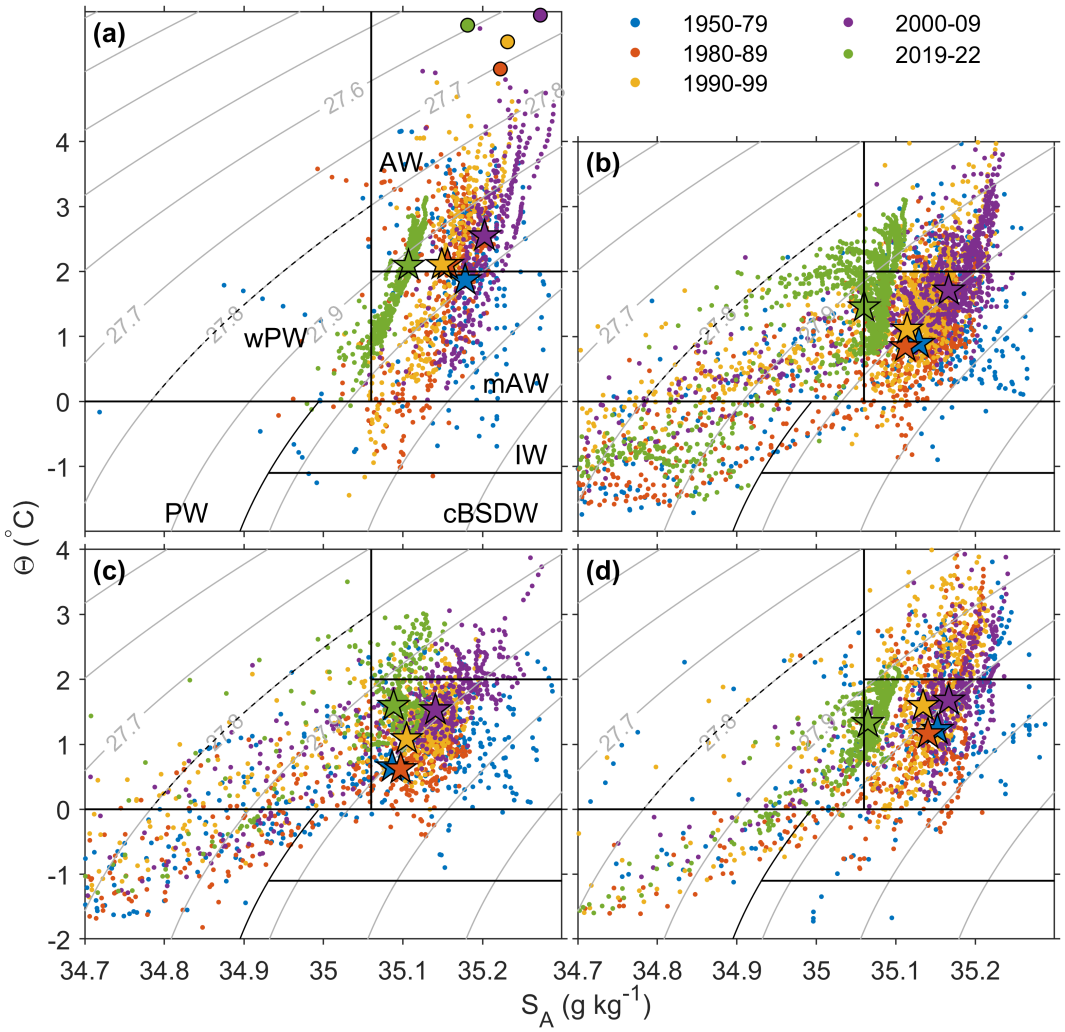

Figure 5. Θ-S_A diagram for **(a)** Section H, **(b)** Section B, **(c)** Section D and **(d)** Section I, including historical and recent data collected between August and February. Contours are σ_0 at 0.1 kg m^{-3} intervals. The upper 50 m of the water column is excluded to remove the short-term variability from atmospheric forcing. Stars show the median value for the respective decade as indicated by the colors. Large circles in (a) show annual mean properties in the BSO between the 50-200 m layer.

directed northwest with an intensified core at the 300 m isobath approaching the slope towards the Great Bank (Figure 4a, Sec G). The flow towards Section G is not always northwestward though, as the depth-averaged objectively mapped field displays currents flowing southeast on the northern side of the section (Figure 4b). This is discussed further in Section 5.1. The northward transport of AW is 0.2 Sv, while it is 0.1 and 0.2 Sv for mAW and wPW respectively (Table 3). At the western edge of Section G, towards the center of the Hopen Trench, less modified AW resides with a surface maximum Θ and subsurface maximum S_A (Figure 3).

Moving further north, Section D provides a comprehensive view of the Hopen Trench, where the inflowing AW is surrounded by PW on both sides (Figure 3, Sec D). The northward transport of AW through Section D amounts to 0.2 Sv, whereas the respective transports for mAW, wPW and PW are 0.3, 0.1, and 0.1 Sv (Table 3). The northward-flowing PW is located on the eastern edge of the section, on the Great Bank shelf break. On the western edge of the section, a cold core current is flowing south, transporting 0.3 Sv, of which 0.1 Sv is PW. The remaining 0.2 Sv is mainly Surface Water (SW) and wPW, hence the net northward transport of AW, mAW and wPW is 0.5 Sv. The northward flowing Atlantic-origin waters show a two-branch structure, with the warmer core observed in the western branch. This suggests either a more direct pathway for the AW along the western side or less mixing along this particular route (Figure 3a and 4a, Sec D). In addition, the water masses found along Section D suggest that the water mass transformation at this higher latitude is influenced more by mixing with PW than atmospheric cooling, in contrast to Section H (Figure 5c).

At the northern edge of the Hopen Trench, a 180-m deep sill separates the AW domain in the south from the PW domain in the Olga Basin in the north (Figure 3a, Sec B). The inflowing Atlantic-origin waters meet the PW on top of the sill generating the PF. The sloping isopycnals across the PF set up a geostrophic flow transporting Atlantic-origin waters and PW eastward along the sill (Figure 4a, Sec B). This eastward flow transport 0.3 Sv and is largely topographically steered. The part of the current north of the highest point on the sill continues northeast along the slope of the Great Bank, while the part south of the sill likely recirculates southeast (Figure 4b). Hence, the amount of Atlantic-origin waters crossing the sill will be largely determined by the position of the front and the width of the frontal current.

4.2 Hydrography and circulation north of the PF from recent observations (2019-2022)

North of the sill, the Olga Basin dominated by PW is situated. The general circulation in the Olga Basin is cyclonic, following the basin slopes (Figure 4b). PW enter the basin from northwest and northeast, on either side of King Karls Land (Figure 4b). The coldest waters are located between the 50 m and 100 m layer, extending to about 150 m depth at the center of the basin (Figure 3, Sec F, A and E). Section F captures the southeastward flowing PW with a volume transport of 0.3 Sv. Including surface waters, the total transport is 0.5 Sv southeastward. Parts of this current continue south as the ESC towards Section D, forming the western reverse flow through Section D and the anticyclonic flow around the Spitsbergen Bank, while parts continue east towards Section A. The transport through section A is 0.5 Sv, of which 0.2 is PW and the rest is mAW and wPW (Table 3). While AW is not present north of the sill, both the mAW and wPW is a result of Atlantic waters flowing northward towards the sill, mixing with PW at the PF near the sill. The AW signature north of the PF is manifested as the subsurface Θ and S_A core hugging the eastern slope of the Olga Basin (Figure 3, Sec. A and E.). Further northeast, through Section E, the northeast transport is 0.5 Sv, where 0.3 is PW and 0.1 Sv is wPW. On the northern side of Section E, the southwestward current transport 0.3 Sv of PW into the Olga Basin. Note however that this inflow of PW from northeast is warmer and saltier than that found along Section F, likely due to AW entering

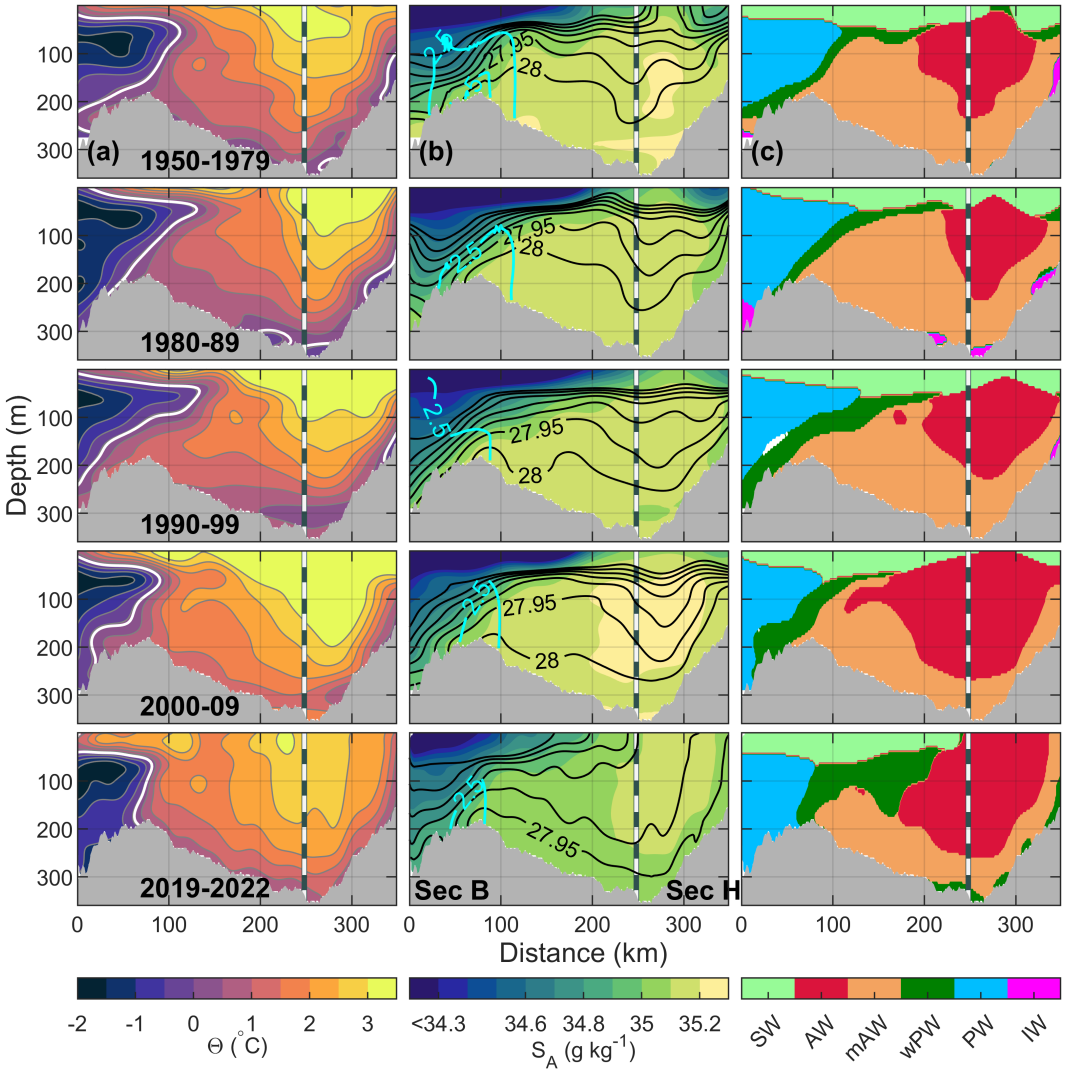

Figure 6. Historical Section B and H averaged over the years indicated in the left panels, only including profiles collected within the months August to February. **(a)** Conservative Temperature, Θ, **(b)** Absolute Salinity, S_A and **(c)** water masses as defined in Table 2. The white line in (a) is the 0.1°C isotherm, indicating the polar front. Black contours in (b) show isopycnals at every 0.05 kg m^{-3} interval starting at 27.7. The cyan contours in (b) show the relative geostrophic velocity in cm s^{-1}, referenced to the surface. Positive values are directed in to the page.

the Barents Sea from the north in addition to AW from the south recirculating in the basin (Figure 3 and Table 4).

4.3 Decadal changes south of the Polar Front

Between 1980 and 2010 the temperature of the AW inflow into the region increases (Figure 6, 7 and 8, and Table 4). Nevertheless, the period between 1950 and 1979 stands out as saltier and warmer than the following 80s most places south of the PF. Next we describe the decadal changes observed along each section.

Table 4. Average water mass properties in sections. Mean Conservative Temperature ($\overline{\Theta}$), Absolute Salinity ($\overline{S_A}$), and percentage of area occupied, A (%), for different water masses and different analysis periods are listed. $\overline{\mathrm{HC}}$ is the average heat content in MJ per volume (1×10^6 J m^{-3}), rounded to the nearest first decimal. $\overline{\mathrm{HC}}$ is calculated for waters deeper than 50 m depth and with temperatures above (below) 0.1°C as described in Section 3.4. Errors in the $\overline{\Theta}$, $\overline{S_A}$ and $\overline{\mathrm{HC}}$ estimates are ±0.1°C, ±0.02 g kg^{-1} and ±0.4 $\times$ 10^6 J m^{-3}, respectively, calculated as described in Section 3.3 and 3.4.

Year	**AW**			**mAW**			**wPW**			**PW**			$\overline{\mathrm{HC}}$
	$\overline{\Theta}$	$\overline{S_A}$	A	$\overline{\Theta}$	$\overline{S_A}$	A	$\overline{\Theta}$	$\overline{S_A}$	A	$\overline{\Theta}$	$\overline{S_A}$	A	
Section H													
1950-79	2.7	35.17	40	1.0	35.17	43	2.0	35.01	5	n/a	n/a	0	7.0 (-0.3)
1980-89	2.8	35.15	43	1.0	35.12	37	1.2	35.02	3	n/a	n/a	0	7.7 (-0.5)
1990-99	3.0	35.16	53	1.0	35.12	35	n/a	n/a	0	n/a	n/a	0	8.1 (-0.6)
2000-09	3.5	35.20	70	1.3	35.17	27	n/a	n/a	0	n/a	n/a	0	10.3 (n/a)
2019-22	2.5	35.11	64	1.5	35.08	30	0.8	35.05	7	n/a	n/a	0	8.1 (n/a)
Section B													
1950-79	2.6	35.16	10	1.2	35.15	44	0.8	35.01	9	-0.9	34.64	22	5.6 (-3.4)
1980-89	2.4	35.14	4	1.1	35.14	49	0.8	34.99	8	-1.0	34.55	26	4.8 (-3.9)
1990-99	2.5	35.15	9	1.3	35.13	41	0.8	34.95	15	-0.7	34.49	20	5.5 (-3.0)
2000-09	2.7	35.18	27	1.7	35.16	32	0.7	34.95	10	-0.8	34.59	17	7.5 (-3.1)
2019-22	2.5	35.09	19	1.4	35.08	25	1.7	35.01	20	-1.0	34.71	20	7.2 (-4.2)
Section D													
1950-79	n/a	n/a	0	1.0	35.15	48	0.8	34.98	14	-0.8	34.69	21	4.1 (-3.3)
1980-89	n/a	n/a	0	0.9	35.11	47	0.6	34.98	12	-0.9	34.62	24	3.5 (-3.9)
1990-99	n/a	n/a	0	1.3	35.13	41	0.8	34.95	17	-0.8	34.47	26	4.8 (-3.3)
2000-09	2.2	35.14	12	1.7	35.15	43	0.9	34.97	12	-0.7	34.63	14	6.7 (-2.8)
2019-22	2.5	35.11	19	1.5	35.10	32	1.1	34.98	9	-0.8	34.72	13	7.4 (-3.3)
Section I													
1950-79	2.4	35.16	16	1.2	35.17	51	0.9	35.00	10	-0.4	34.83	6	5.7 (-1.1)
1980-89	2.5	35.16	19	1.1	35.14	52	0.8	35.02	6	-0.7	34.79	5	5.6 (-2.7)
1990-99	2.7	35.15	31	1.2	35.12	40	1.0	34.99	6	-0.7	34.69	4	7.0 (-2.7)
2000-09	2.7	35.18	27	1.4	35.16	49	0.9	34.99	6	-0.3	34.85	1	6.9 (-1.0)
2019-22	2.0	35.08	5	1.5	35.08	49	1.2	35.02	36	-0.7	34.78	7	5.7 (-2.9)
Section F													
2019-22	n/a	n/a	0	n/a	n/a	0	0.2	35.00	3	-1.0	34.68	75	1.0 (-4.4)
Section A													
2019-22	n/a	n/a	0	1.1	35.07	3	0.6	34.98	15	-0.9	34.74	63	3.0 (-3.9)
Section E													
2019-22	n/a	n/a	0	0.7	35.08	1	0.2	34.92	12	-0.6	34.70	68	1.5 (-2.2)

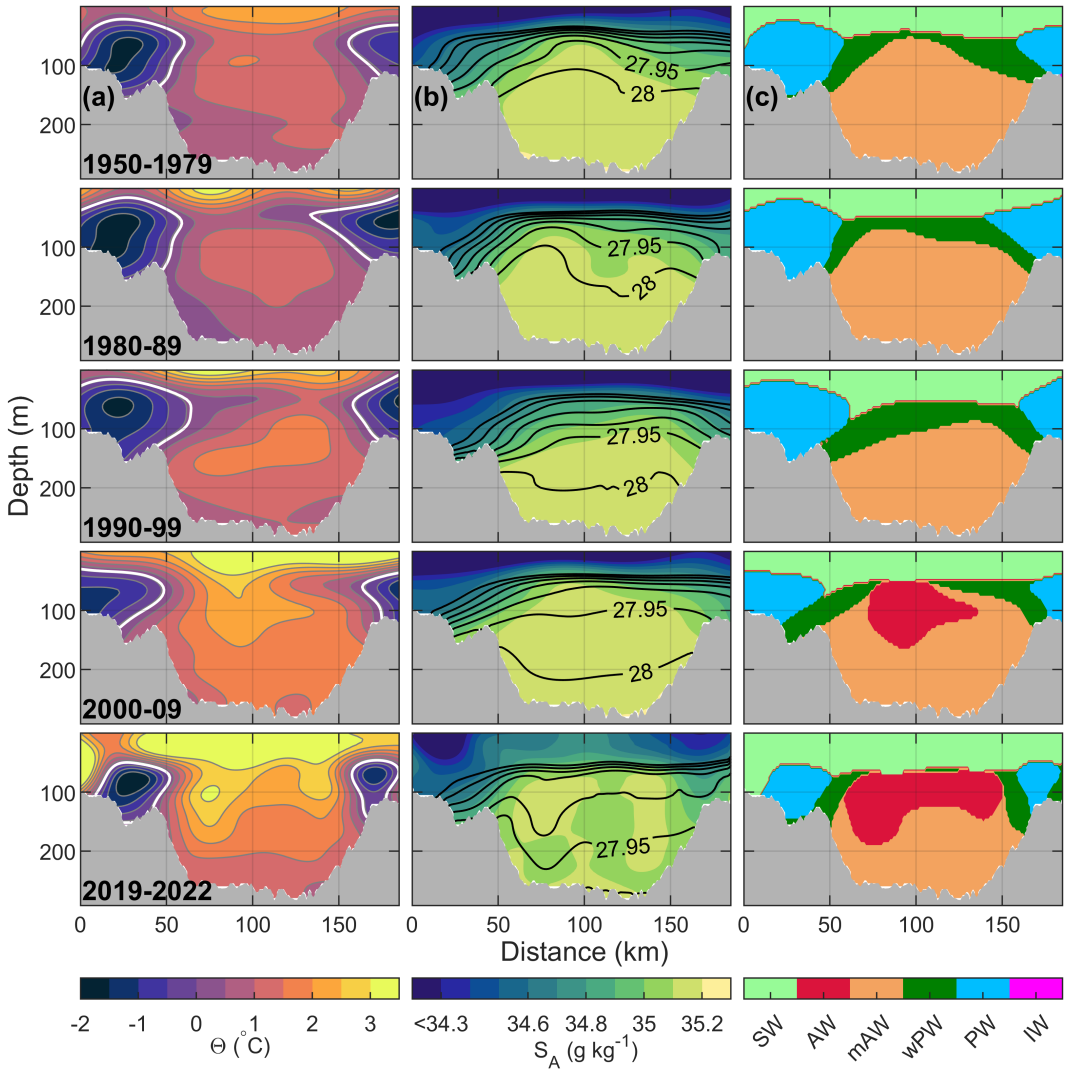

Figure 7. Same as Fig. 6 but for Section D.

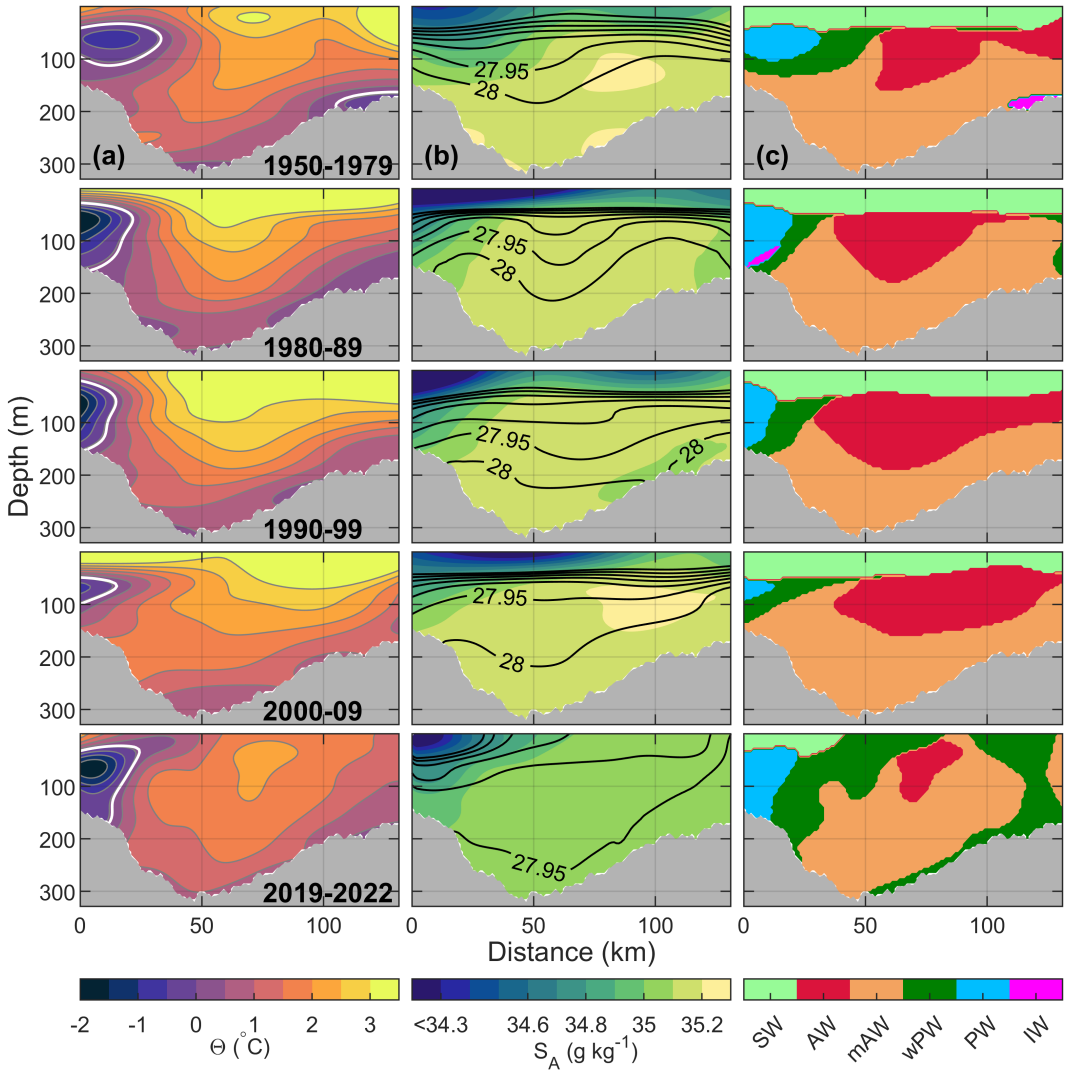

Figure 8. Same as Fig. 6 but for Section I.

The AW inflow into Section H was on average 2.7°C in 1950-79, increasing to a maximum of 3.5°C in the 2000s (Table 4). The increase in temperature resulted in a transition from about 40% of the water mass being mAW before the 90s to less than 30% in the 2000s (Figure 6c and Table 4). The corresponding AW fraction increased from 40% to 70% in the same period. The transition towards more AW from pre 90s to the 2000s is observed along all sections south of the PF (Table 4). Particularly along Section B and D, AW has manifested after the 2000s where it was hardly present before. Correspondingly, the heat content per volume, HC, increased by $3.3\,\mathrm{MJ\,m^{-3}}$ (50%) between 1950 and 2010 along Section H, while it increased by 1.9 (30%), 2.6 (60%) and $1.2\,\mathrm{MJ\,m^{-3}}$ (20%) along Sections B, D and I, respectively. This difference in increased heat content between different sections south of the PF is likely a result of the dynamics in the region, and is discussed in Section 5.2. Note that for Section B, D and I, the 80s stand out as the coldest decade (Table 4).

While the temperature of the AW inflow has increased through the decades, the change in salinity is not as pronounced. Both the 80s and 90s indicate a fresher AW and particularly mAW inflow than in the 1950-79 period, while the 2000s stand out as anomalously saline (Table 4 and Figure 5). Our recent data (2019-22) however stand out as anomalously fresh, with the AW inflow being as much as $0.06\,\mathrm{g\,kg^{-1}}$ fresher than observed in the previous decades (Table 4 and Figure 5a). While the reason for the recent freshening is due to downstream conditioning addressed in Section 5.2, the implications are seen along all sections south of the PF where the density in general is about $0.05\,\mathrm{kg\,m^{-3}}$ less than in the previous decades (Figures 5, 6b, 7b and 8b). As a result, the Atlantic-origin waters reaching the top of the sill in the northern part of Section B do not subduct below the PW as readily as in previous decades (Figure 6). The PF is relatively steeper, effectively reducing the amount of Atlantic-origin waters entering the Olga Basin below 100 m depth. In addition, the geostrophic flow along the front on top of the sill is at its weakest during the 2019-22 period compared to the previous decades (Figure 3b, pink contours). The reduction in the geostrophic flow is caused by a decreased density gradient across the front.

While the AW density in the Hopen Trench is observed to be anomalously low in the 2019-2022 period, our decadal average of historical observations suggest the AW density has been decreasing since the 80s due to increasing temperatures (Figure 5). The decreasing AW density in the Hopen Trench is likely the reason for the observed weakening of the along front geostrophic flow since the 50s (Figure 3b). In addition, the decreasing AW density result in less dense water production when mixing with PW. While IW could be found along the different sections before 2000, it is absent after (Figure 5).

4.4 Decadal changes north of the Polar Front

PW is the dominant water mass north of the PF in the Olga Basin, on the Great Bank, and along the 100 m isobath on the Spitsbergen Bank (Figures 3 and 9). Here the Olga Basin is defined as the basin within the 200 m isobath, between 77.4 and 78.5°N and west of 33°E. The largest changes in the distribution of PW between the 50s and present day can be observed along the Spitsbergen Bank south of 77°N (Figure 9). The area on the Spitsbergen Bank occupied by waters colder than 0.1°C (averaged over the 50-100 m layer) was about $20 \times 10^3\,\mathrm{km^2}$ between 1950-79, while only $12 \times 10^3\,\mathrm{km^2}$ in the 2000-09 period (Figure 9). The corresponding change in the average temperature for the same area was an increase from -0.7 ± 0.1°C to -0.4 ± 0.1°C. This reduction in area occupied by Arctic-origin waters is likely a result of the increased temperatures of the Atlantic-origin waters, flowing in on both the eastern and western sides of the Spitsbergen Bank (Figure 9). Below 100 m depth on the Spitsbergen Bank, the temperature has increased even more than within the 50-100 m layer. From the 80s to 2000s, the average heat content per volume increased from $-3.5 \pm 0.4 \times 10^6\,\mathrm{J\,m^{-3}}$ to $0.6 \pm 0.4 \times 10^6\,\mathrm{J\,m^{-3}}$, equivalent to a temperature increase of 0.7°C.

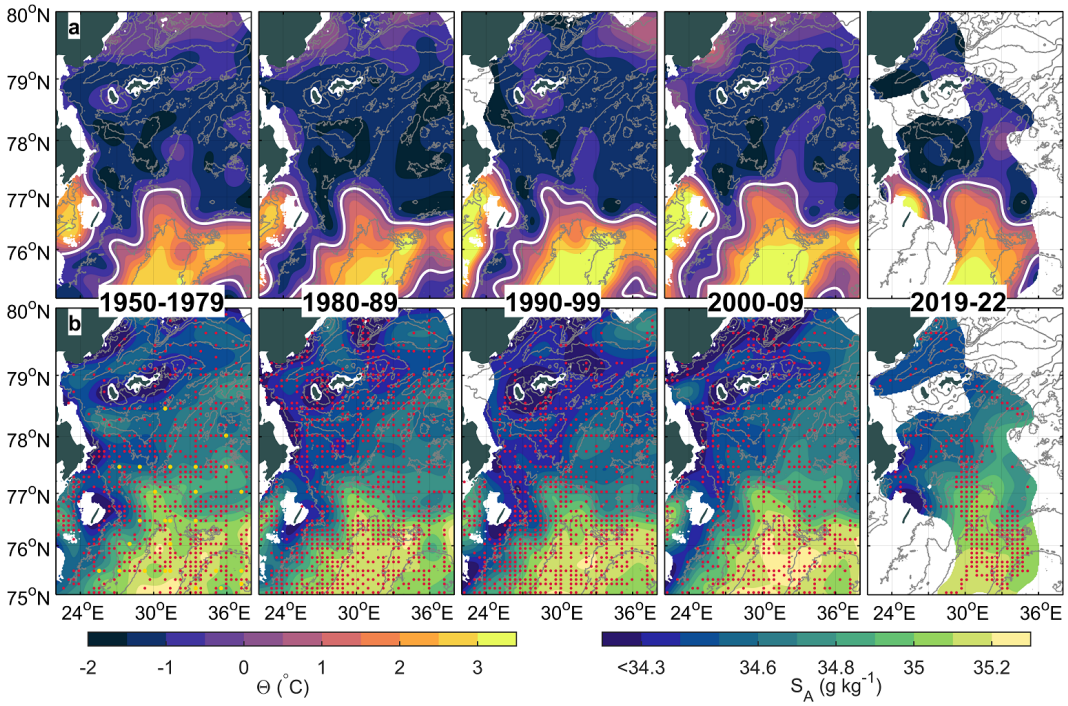

Figure 9. **(a)** Conservative Temperature, Θ, and **(b)** Absolute Salinity, S_A, averaged over the 50-100 m layer and objectively mapped for the different time periods as described in Section 3.5. Only profiles within the period August to February are included. Red dots in (b) indicate 10 by 10 km bins where we have data. Yellow dots in the 1950-1979 panel indicate where we have binned profiles that covers the water column deeper than 100 m.

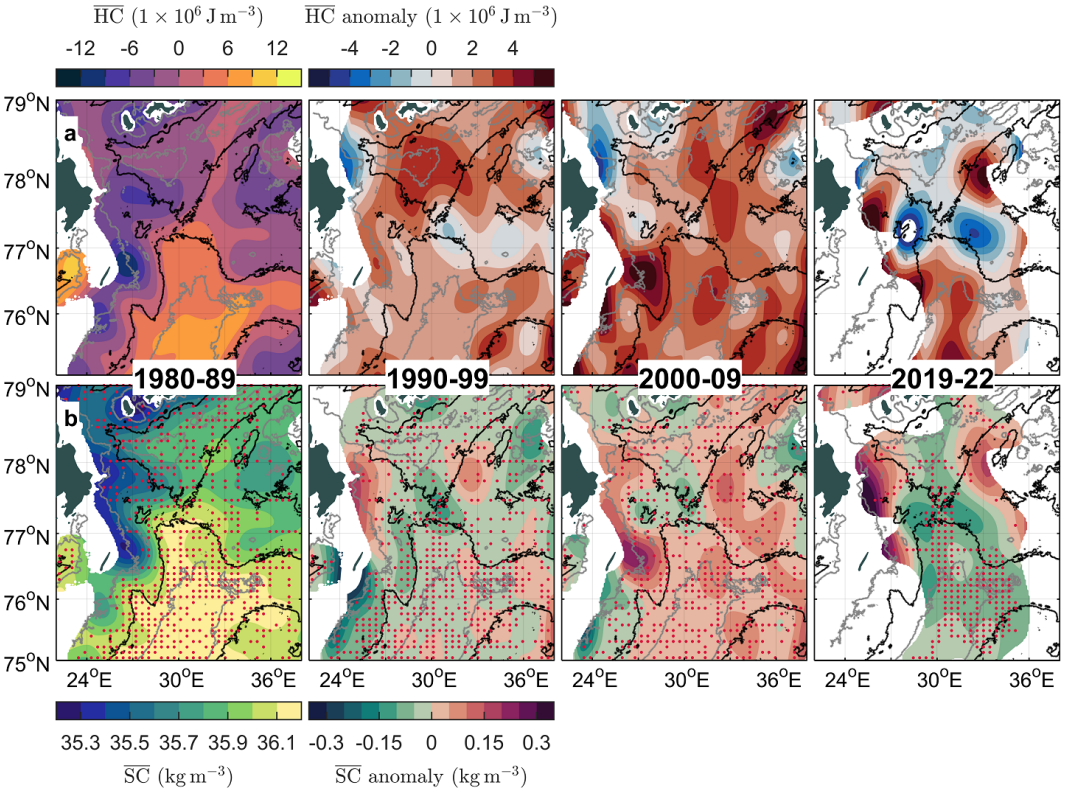

Figure 10. **(a)** Average heat content per volume, $\overline{\text{HC}}$, and **(b)** average salt content per volume, $\overline{\text{SC}}$, for the time period 1980-89, below 100 m depth. For the following time periods, heat content anomalies and salt content anomalies per volume are displayed in the upper and lower rows, respectively. Only profiles within the period August to February are included. Red dots in (b) indicate 10 by 10 km bins where we have data. Black line is the 200 m isobath while gray lines show the 100 m and 300 m isobaths.

In the Olga Basin, the 80s and 90s stand out as the coldest and warmest decades, respectively, although the variations are small with average temperatures ranging between -1.4 ± 0.1°C and -1.3 ± 0.1°C (Figure 9). The 90s also stand out as the period with the freshest PW within the Olga Basin, with an average salinity of $34.41 \pm 0.02\,\mathrm{g\,kg^{-1}}$, while our observations between 2019-22 show the saltiest PW with an average salinity of $34.59 \pm 0.02\,\mathrm{g\,kg^{-1}}$. Below 100 m depth, the main pathway of Atlantic-origin waters is visible as water with higher heat content following the 200 m isobath along the basin (Figure 10). Note that the heat content below 100 m depth is not presented for the 1950-79 period as we had few CTD profiles covering the entire water column in this period, as indicated by yellow dots in Figure 9b. From the 80s to the 2000s, the average heat content per volume below 100 m depth increased from $-2.1 \pm 0.4 \times 10^6\,\mathrm{J\,m^{-3}}$ to $0.0 \pm 0.4 \times 10^6\,\mathrm{J\,m^{-3}}$, equivalent to an increase in temperature of 0.5°C (Figure 10). The deep Olga Basin was at its warmest in the 90s when the average heat content was $0.8 \pm 0.4 \times 10^6\,\mathrm{J\,m^3}$, while it was at its saltiest in the 2000s when the average salt content per volume was $35.79 \pm 0.02\,\mathrm{kg\,m^{-3}}$ (equivalent to a $0.03\,\mathrm{g\,kg^{-1}}$ increase in S_A from the 90s).

On the Great Bank, defined as the region above the 200 m isobath between 76°N and 77°N and east of 33°E, the 80s stand out as colder and fresher than the previous 1950-79, with an average temperature and salinity of -1.4 ± 0.1°C and $34.68 \pm 0.02\,\mathrm{g\,kg^{-1}}$ respectively, within the 50-100 m layer (Figure 9). After the 80s, temperatures both in the 50-100 m layer and below 100 m depth increased to a maximum in the 2000s. The increased heat content on the Great Bank in the 2000s coincides with a broadening of the PF region on the sill at the northern edge of the Hopen Trench, with Atlantic-origin waters maintaining its heat signature further northeast along the 200 m isobath than in previous decades (Figure 9).

5 Discussion

5.1 Atlantic Water pathways in the western Barents Sea

The main AW path into the Barents Sea is through the Bear Island Trough. Excluding the Norwegian Coastal Current, the annual mean inflow is 2 Sv, and 2.1 Sv when averaged over August to February (Smedsrud et al., 2010). A fraction of the inflow recirculates and leaves the Barents Sea as a westward flowing current south of the Bear Island (Gawarkiewicz & Plueddemann, 1995; Skagseth, 2008; Smedsrud et al., 2010). The volume transport of the westward current is 1.2 Sv; however, how much of this is recirculating AW and how much is Arctic -origin waters is not known (Gawarkiewicz & Plueddemann, 1995; Smedsrud et al., 2010). In Figure 11 we summarize the inferred pathways and volume transport estimates from the observations synthesized in this study. We observe the inflow at Section H to be 0.9 ± 0.1 Sv, suggesting that half of the AW inflow through the BSO reaches the Hopen Trench (Table 3 and Figure 11).

From Section H, the current divides at the 300 m isobath where the upper branch continues into the Persey Trench (0.5 Sv) while the lower branch continues northward (0.5 Sv). At Section G, the u_g core flows northwestward, centered at the 300 m isobath, co-located with a surface Θ maximum (Figure 3a and 4a, Sec G). This is contrary to the observations made by Våge et al. (2014), where they observed currents flowing southeast in nearly the same location during a week in August 2007. Our geostrophic velocity fields are based on three glider transects conducted during December and January, and one reason for the discrepancy could be a seasonal change (Figure 2). In fact, our objectively mapped currents based on SADCP, LADCP and DAC do suggest that currents at times flow southeast across Section G (Figure 4b). This is however, a region where tidal currents may exceed $20\,\mathrm{cm\,s^{-1}}$ (Fer & Drinkwater, 2014). Extracting the mean flow of $< 10\,\mathrm{cm\,s^{-1}}$ through detiding of individual SADCP transects and LADCP profiles may have uncertainties with comparable magnitude and must be interpreted with caution. In addition, Våge et al. (2014) states that the circulation south of the PF in the

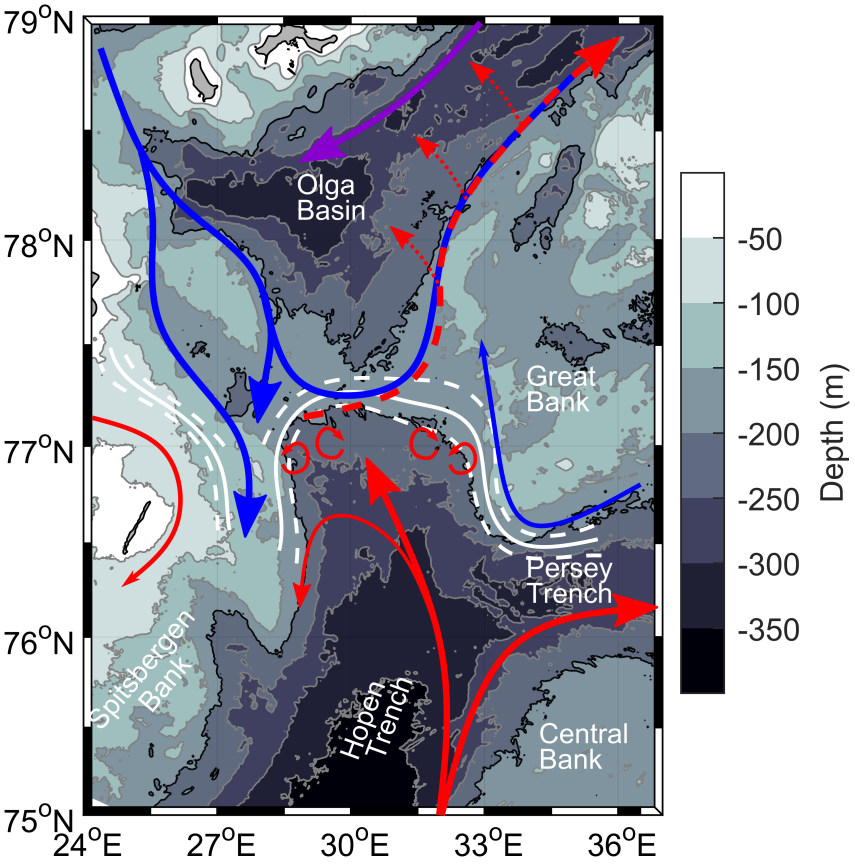

Figure 11. Mean currents of Atlantic Water (red) and Polar Water (blue) in our study region, as inferred from our observations between 2019 and 2022. Red dashed line indicate subducted Atlantic-origin waters. Purple line is PW that has a higher heat content than PW in the west, due to mixing with AW inflow. White solid line marks the mean position of the polar front based on historical and recent data, with the white dashed lines indicating one standard deviation.

Barents Sea is too complex to be conclusively described by individual surveys, as sea level, tidal flows and winds change the dynamics of the front.

Section D is characterized by a three-branch structure flowing northward and a one branch flowing southwards (Figure 4a). The two branches on the either side, located on the shelves, are mainly composed of Polar-origin water, where PW flow north on the Great Bank shelf, and south on the Spitsbergen Bank (Figures 3 and 4a). The two branches in the Hopen Trench consist of Atlantic-origin waters, and are hereby referred to as the western and eastern branches of Section D (Figure 3 and 4). The volume transport estimates of the western and eastern branches are 0.5 Sv and 0.2 Sv, respectively. Hence, the total northward transport by these two branches is 0.7 Sv, exceeding the transport estimates through Section G and the lower branch of Section H. This suggests the northward transport is not fully captured by Section H and G. Note that there is a seasonal difference in when we have data along Section D compared to Section H and G. We only collected data along Section D during the October cruises, whereas the gliders collected data along Section G and H mainly during late fall and winter (Figure 2 and Table 1). However, we expect more AW inflow in late fall and winter compared to October (Smedsrud et al., 2010), hence the observed discrepancy between Section D and Sections H and G is likely not due to seasonality. Instead, the western branch in Section D is warmer than the eastern one, suggesting a more direct route or less mixing along the route than through Section G. We hypothesize that the eastern branch in Section D is the branch also observed in Section G, and that the western branch in Section D flows north from Section H more or less parallel to Section B.

Another possibility is that this western branch in Section D comes from a retrograde current flowing northeast along the Spitsbergen Bank slope such as described by Loeng (1991) and Li and McClimans (1998). While our three SADCP transects across the Spitsbergen Bank slope would contradict this (Figure 2b and 4b) we can not exclude this as a possibility. Nevertheless, such a retrograde current is unlikely to follow the Spitsbergen Bank all the way from the BSO as several studies report westward flowing currents along the southern Spitsbergen Bank (Gawarkiewicz & Plueddemann, 1995; Parsons et al., 1996; Skagseth, 2008).

Barton et al. (2018) suggest that AW flows clockwise around the Hopen Trench due to potential vorticity constraints in a basin with a shallower northern outflow depth than inflow. This could be true for the Hopen Trench where parts of the AW entering from the south eventually flows across the sill at the northern edge of the Hopen Trench, continuing into the Olga Basin. Hence it is possible that the western branch in Section D comes from AW flowing more or less straight north from Section H, shifting from following the right hand slope to the left hand slope. The dynamics involved in such a transition requires further study.

At the sill between the Hopen Trench and the Olga Basin, a geostrophic frontal current flowing east develops due to the density difference between the AW and PW (Figure 4, Sec B and 6b). We observe a decrease in the relative geostrophic velocity along the front during the decades, in addition to a northward shift of the core of this current (Figure 6b). These changes to the frontal current are caused by the change in Θ and S_A of the PW and AW (discussed in Section 5.2), and effectively determines how much Atlantic-origin waters may cross the sill. A weakening of the frontal current suggests less Atlantic-origin water flow along the front. Yet, a northward shift suggests more Atlantic-origin water are topographically steered along the northern side of the Great Bank instead of the southern side. The PF is a site for rapid mixing between Atlantic-origin waters and Polar-origin waters, yet the dynamics of the PF and the frontal current is a topic for another ongoing study and will not be addressed in depth here. The frontal jet observed during our 2019-2022 observations continues towards Section A and E where the heat signature of Atlantic-origin waters is still present. Atlantic-origin waters flowing across

the sill at the northern edge of the Hopen trench is supported by model studies such as Aksenov et al. (2010).

5.2 Change in heat and salt content

Between 1980 and 2010 we observe a warming of the AW along all Sections south of the PF (Table 4 and Figures 6, 7, 8). Correspondingly, the area occupied by Atlantic water is expanding, in agreement with the process of Atlantification reported by numerous studies (Skagseth et al., 2008; Smedsrud et al., 2010; Årthun et al., 2012; Onarheim et al., 2014; Oziel et al., 2016; Barton et al., 2018; Ingvaldsen et al., 2021). The increase in area occupied by AW is mainly due to a shift from mAW to AW because of the increased temperatures in the AW inflow. This is supported by time series showing the increase in AW temperatures through the BSO since the 80s (Skagseth et al., 2008). As a result, the temperature gradient across the polar front along Section B has increased since the 80s, and the PF position, the location of the 0.1°C isotherm between 50-100 m has shifted about 50 km north (Figure 6). However, the change in the PF position is not only a result of increased AW temperatures. From the 80s to the 90s, the heat content south of the PF increased without it changing the position of the front. Instead, more AW flowed towards the sill under the PW due to fresher PW north of the sill within the Olga Basin (Figures 9 and 10). The fresh PW layer in the Olga Basin observed in the 90s is supported by observations by Lind et al. (2018). We speculate that this caused the Olga Basin to be record warm in the 90s according to our historical observations. In the following 2000s AW reached a record high temperature and salinity south of the PF, however, as the Olga Basin also had a higher salt content in the 2000s, thus being denser, the AW inflow was instead directed east onto and along the Great Bank (Figures 9 and 10). The core of the geostrophic frontal current was stronger and located further south in the 2000s compared to the 90s, supporting an eastward shift of the Atlantic-origin waters (Figure 6b). We hypothesize that the relative density of the PW within the Olga Basin compared to that of the AW south of the PF effectively regulate how much AW is able to enter the Olga Basin from the Hopen Trench. A reduction in density south of the front compared to that in the Olga Basin will reduce the AW inflow.

Our observations from the 2019-2022 period show that the AW inflow is anomalously fresh. This is due to upstream conditions and is also observed in the annual mean properties of the AW inflow through the BSO (Figure 5a). This anomalously fresh AW inflow can be linked to the largest freshening event for 120 years in the North Atlantic and can be traced along the Norwegian coast (Holliday et al., 2020). The annual mean properties across BSO are plotted in Figure 5a and show how the 2019-2022 period stands out as about $0.05\,\mathrm{g\,kg^{-1}}$ fresher than the 80s and 90s and nearly $0.1\,\mathrm{g\,kg^{-1}}$ fresher than the 2000s. As a result, the AW south of the front is about $0.05\,\mathrm{kg\,m^{-3}}$ less dense than in previous decades, and the amount of warm water extending northward under the PW across the PF is reduced (Figure 6). Hence, if the temperature of the AW inflow continues to increase without an increase in AW salinity to compensate for the density loss, the result will be that less Atlantic-origin water is able to cross the PF. In addition, even if the Atlantification of the Olga Basin continues as speculated by Lind et al. (2018), we hypothesize that an increased salinity in the Olga Basin will serve as a negative feedback mechanism, slowing down the Atlantification.

Another effect of the anomalously fresh AW inflow is the reduced dense water production. Reduced cooling of AW by the atmosphere in the Barents Sea is already causing warmer water to reach the PF, mixing directly with PW. However, until 2018 the increased AW temperature was largely compensated for by increased salinity (Skagseth et al., 2020). The recent freshening of the AW causes water masses produced by mixing AW with PW to be less dense (Figure 5). This is exactly what was suggested by Skagseth et al. (2020) and may have far reaching consequences for the general dense water production in the Barents Sea.

6 Conclusions

This study investigates the characteristics and dynamics of the AW and PW in the western Barents Sea. Observations from three scientific cruises and nine glider missions conducted in the Barents Sea between 2019 and 2022 are synthesized to describe the present conditions. In addition, historical data collected after 1950 are averaged over decades and compared to recent observations.

We present detailed circulation pathways of Atlantic- and Polar-origin waters in a region essential for water mass transformation and poleward transport of heat and salt (Figure 11). 0.9 ± 0.1 Sv of Atlantic-origin water reaches the Hopen Trench between Spitsbergen Bank and Central Bank (Figure 4 and Tabel 3). This is about half of the AW inflow through the BSO. The AW inflow into the Hopen trench bifurcates; one branch flowing east along the Persey Trench and one continuing north along the Hopen Trench. Each of the two branches transport about 0.5 Sv of Atlantic-origin waters. At the northern edge of the Hopen Trench, AW eventually subducts under the PW and the PF, continuing northward along the eastern slope of the Olga Basin as a topographically steered current.

PW is entering the Olga Basin from northeast and northwest (Figure 4 and Figure 11). These two branches are of similar magnitude as the AW inflow, transporting 0.5 Sv each. The northwestern branch is the colder one, containing more PW than the northeastern branch. The difference in heat content between the two branches ($2.2 \times 10^6\,\mathrm{J\,m^{-3}}$, Table 4) is due to recirculating AW within the eastern Olga Basin, and AW entering from the north (Lundesgaard et al., 2022).

The AW is undergoing continuous modifications along its pathway. Upstream of the Hopen Trench, AW transformation is primarily influenced by cooling from the atmosphere, while along the Hopen Trench and Persey Trench the transformation is mainly driven by mixing between AW and PW (Figure 5).

We observe a warming of the AW inflow between 1980 and 2010 south of the PF, where the AW heat content increased by 50% in this period. The increase in temperature causes water mass distribution to shift from mAW being the dominant water mass to AW taking over (Figures 6, 7 and 8).

The increasing AW heat content south of the PF can be traced along the AW pathway under the PF into the Olga Basin. However, we hypothesize that the amount of warm water crossing the PF and the topographic sill separating AW from PW is regulated by the density difference between AW south of the sill and PW in the Olga Basin. Our observations indicate the Olga Basin cooled from the 90s to the 2000s even though the AW temperature south of the sill continued to increase. This was likely a result of denser waters residing in the Olga Basin due to increased salinity.

Our recent observations show that the salinity of the AW inflow reduced by nearly $0.1\,\mathrm{g\,kg^{-1}}$ from the 2000s to the 2019-2022 period, reducing the AW density south of the PF by as much as $0.05\,\mathrm{kg\,m^{-3}}$. As a result, mixing of AW with PW produced less dense water, the temperature gradient across the PF increased, and less warm water was able to flow north under the PW (Figure 6, 9 and 10).

Finally, we observe that the area occupied by waters colder than 0.1°C on the Spitsbergen Bank has reduced by 40% since the 1950s. With the increasing temperatures in the AW inflow both south and north of the Spitsbergen Bank, we speculate that southward flowing PW along the Spitsbergen Bank may eventually be blocked off by AW converging from west and east, at around 77°N.

While this study has provided valuable insights into the circulation and dynamics of AW and PW in the western Barents Sea, further research is warranted to deepen

our understanding of this complex system. Future investigations should aim to incorporate longer time series combined with high-resolution data to capture the intricacies and variability of the AW inflow, as well as its interactions with other components of the regional climate system.

7 Open Research

In this study we use data collected as part of the Nansen Legacy project. This includes five glider missions conducted between 2019 and 2021 (E. Kolås, 2022), CTD and MSS data from RV G.O. Sars collected in October 2020 (Fer, Skogseth, et al., 2023; Fer, Baumann, Elliot, & Kolås, 2023), MSS data from RV Kronprins Haakon collected in February 2021 (Fer, Baumann, Kalhagen, et al., 2023), and MSS data from RV Kristine Bonnevie collected in October 2022 (Fer, Baumann, Hana, et al., 2023). Data from the glider missions conducted between 2021 and 2022 and the CTD/LADCP/SADCP data from the February 21 and October 22 cruises are being prepared for publication and will be submitted during the review process.

Additional data used are SADCP data from several different Nansen Legacy cruises. (Cannaby et al., 2022), historical CTD profiles from the UNIS hydrographic database (Skogseth et al., 2019), bathymetry data from the International Bathymetric Chart of the Arctic Ocean (IBCAO), version 4 (Jakobsson et al., 2020), and sea surface temperature from the product SEAICE_ARC_SEAICE_L4_NRT_OBSERVATIONS_011_008 at 0.05° resolution based upon observations from the Metop_A AVHRR instrument.

Acknowledgments

This work was supported by the Nansen Legacy Project, project number 276730. We thank the officers, crew and scientist of the RV G.O. Sars cruise in October 2020, RV Kronprins Haakon in February 2021 and RV Kristine Bonnevie cruise in October 2022. We thank the glider team at NorGliders (http://norgliders.gfi.uib.no/), for operating and maintaining all the glider missions in challenging conditions in the Barents Sea.

References

Aksenov, Y., Bacon, S., Coward, A. C., & Nurser, A. J. G. (2010, January). The North Atlantic inflow to the Arctic Ocean: High-resolution model study. *Journal of Marine Systems*, *79*(1), 1–22. Retrieved 2023-06-18, from https://www.sciencedirect.com/science/article/pii/S0924796309002115 doi: 10.1016/j.jmarsys.2009.05.003

Barton, B. I., Lenn, Y.-D., & Lique, C. (2018, August). Observed Atlantification of the Barents Sea Causes the Polar Front to Limit the Expansion of Winter Sea Ice. *Journal of Physical Oceanography*, *48*(8), 1849–1866. Retrieved 2020-02-24, from http://journals.ametsoc.org/doi/10.1175/JPO-D-18-0003.1 doi: 10.1175/JPO-D-18-0003.1

Baumann, T. M., Fer, I., Koenig, Z., Randelhoff, A., Rieke, O., Hana, I., & Årvik, A. (2023, February). Polar Front Process Cruise 2022: Cruise Report. *The Nansen Legacy Report Series*(39). Retrieved 2023-04-18, from https://septentrio.uit.no/index.php/nansenlegacy/article/view/6982 (Number: 39) doi: 10.7557/nlrs.6982

Cannaby, H., Ingvaldsen, R., Reigstad, M., Søreide, J., Gerland, S., Ludvigsen, M., & Fransson, A. (2022). *Vessel mounted Acoustic Doppler Current Profiler data collected in the Barents Sea and adjacent Arctic Ocean by the Norwegian research icebreaker R/V Kronprins Haakon, during 7 individual surveys conducted for the Nansen Legacy project.* Institute of Marine Research. Retrieved from http://metadata.nmdc.no/metadata-api/landingpage/

3e03daeeb8c946786104b01099db5a34 doi: 10.21335/NMDC-1175579976

Fer, I., Baumann, T., Elliot, F., & Kolås, E. (2023). *Ocean microstructure measurements using an MSS profiler during the Nansen Legacy cruise, GOS2020113, October 2020.* University of Bergen. Retrieved 2023-04-18, from http://metadata.nmdc.no/metadata-api/landingpage/efb5d2e2d1f5b147ad828aa48b337205 doi: 10.21335/NMDC-239170563

Fer, I., Baumann, T., Hana, I., Koenig, Z., Randelhoff, A., Rieke, O., & Årvik, A. (2023). *Ocean microstructure measurements using an MSS profiler during the Nansen Legacy cruise, KB2022625, October 2022.* University of Bergen. Retrieved 2023-04-18, from http://metadata.nmdc.no/metadata-api/landingpage/17dc16e9dbe5412c31b1ba86c996ccee doi: 10.21335/NMDC-1169583367

Fer, I., Baumann, T., Kalhagen, K., Koenig, Z., & Kolås, E. (2023). *Ocean microstructure measurements using an MSS profiler during the Nansen Legacy cruise, KH2021702, February 2021.* University of Bergen. Retrieved 2023-04-18, from http://metadata.nmdc.no/metadata-api/landingpage/1a5407acf9bacf7edea36b344c03b631 doi: 10.21335/NMDC-1939445412

Fer, I., Bosse, A., & Dugstad, J. (2020, June). Norwegian Atlantic Slope Current along the Lofoten Escarpment. *Ocean Science*, *16*(3), 685–701. Retrieved 2022-08-18, from https://os.copernicus.org/articles/16/685/2020/ (Publisher: Copernicus GmbH) doi: 10.5194/os-16-685-2020

Fer, I., & Drinkwater, K. (2014, February). Mixing in the Barents Sea Polar Front near Hopen in spring. *Journal of Marine Systems*, *130*, 206–218. Retrieved 2023-06-18, from https://www.sciencedirect.com/science/article/pii/S092479631200022X doi: 10.1016/j.jmarsys.2012.01.005

Fer, I., Skogseth, R., Astad, S., Baumann, T., Elliot, F., Falck, E., ... Kolås, E. (2023). *Ocean hydrography and current profiles from the Nansen Legacy cruise to the northern Barents Sea, GOS2020113, October 2020.* University of Bergen. Retrieved 2023-04-18, from http://metadata.nmdc.no/metadata-api/landingpage/0b8529c10023b9cde2187c9552b553b6 doi: 10.21335/NMDC-1752779505

Fer, I., Skogseth, R., Astad, S. S., Baumann, T., Elliott, F., Falck, E., ... Kolås, E. H. (2021, April). SS-MSC2 Process cruise/mooring service 2020: Cruise Report. *The Nansen Legacy Report Series*(20). Retrieved 2022-09-07, from https://septentrio.uit.no/index.php/nansenlegacy/article/view/5798 (Number: 20) doi: 10.7557/nlrs.5798

Firing, E., & Ranada, J. (1995). *Processing ADCP data with the CODAS software system version 3.1.* Joint Institute for Marine and Atmospheric Research, University of Hawaii and National Oceanographic Data Center., Bremerhaven, PANGAEA.

Frajka-Williams, E., Eriksen, C. C., Rhines, P. B., & Harcourt, R. R. (2011). Determining Vertical Water Velocities from Seaglider. *Journal of Atmospheric and Oceanic Technology*, *28*(12), 1641–1656. doi: 10.1175/2011jtecho830.1

Garau, B., Ruiz, S., Zhang, W. G., Pascual, A., Heslop, E., Kerfoot, J., & Tintoré, J. (2011). Thermal Lag Correction on Slocum CTD Glider Data. *Journal of Atmospheric and Oceanic Technology*, *28*(9), 1065–1071. doi: 10.1175/jtech-d-10-05030.1

Gawarkiewicz, G., & Plueddemann, A. J. (1995). Topographic control of thermohaline frontal structure in the Barents Sea Polar Front on the south flank of Spitsbergen Bank. *Journal of Geophysical Research: Oceans*, *100*(C3), 4509–4524. Retrieved 2022-08-18, from https://onlinelibrary.wiley.com/doi/abs/10.1029/94JC02427 (_eprint: https://onlinelibrary.wiley.com/doi/pdf/10.1029/94JC02427) doi: 10.1029/94JC02427

Holliday, N. P., Bersch, M., Berx, B., Chafik, L., Cunningham, S., Florindo-

López, C., ... Yashayaev, I. (2020, January). Ocean circulation causes the largest freshening event for 120 years in eastern subpolar North Atlantic. *Nature Communications*, *11*(1), 585. Retrieved 2023-06-20, from https://www.nature.com/articles/s41467-020-14474-y (Number: 1 Publisher: Nature Publishing Group) doi: 10.1038/s41467-020-14474-y

Ingvaldsen, R. B. (2005). Width of the North Cape Current and location of the Polar Front in the western Barents Sea. *Geophysical Research Letters*, *32*(16). Retrieved 2023-03-30, from https://onlinelibrary.wiley.com/doi/abs/10.1029/2005GL023440 (_eprint: https://onlinelibrary.wiley.com/doi/pdf/10.1029/2005GL023440) doi: 10.1029/2005GL023440

Ingvaldsen, R. B., Assmann, K. M., Primicerio, R., Fossheim, M., Polyakov, I. V., & Dolgov, A. V. (2021, December). Physical manifestations and ecological implications of Arctic Atlantification. *Nature Reviews Earth & Environment*, *2*(12), 874–889. doi: 10.1038/s43017-021-00228-x

IOC, SCOR, & IAPSO. (2010). *The international thermodynamic equation of seawater – 2010: Calculations and use of thermodynamic properties* (Intergovernmental Oceanographic Commission, Manuals and Guides No. 56 ed.). UNESCO.

Jakobsson, M., Mayer, L. A., Bringensparr, C., Castro, C. F., Mohammad, R., Johnson, P., ... Zinglersen, K. B. (2020, July). The International Bathymetric Chart of the Arctic Ocean Version 4.0. *Scientific Data*, *7*(1), 176. doi: 10.1038/s41597-020-0520-9

Johannesen, E., Ingvaldsen, R. B., Bogstad, B., Dalpadado, P., Eriksen, E., Gjøsæter, H., ... Stiansen, J. E. (2012, July). Changes in Barents Sea ecosystem state, 1970–2009: climate fluctuations, human impact, and trophic interactions. *ICES Journal of Marine Science*, *69*(5), 880–889. Retrieved 2022-08-17, from https://doi.org/10.1093/icesjms/fss046 doi: 10.1093/icesjms/fss046

Johannessen, O. M., & Foster, L. A. (1978). A note on the topographically controlled Oceanic Polar Front in the Barents Sea. *Journal of Geophysical Research: Oceans*, *83*(C9), 4567–4571. Retrieved 2022-08-18, from https://onlinelibrary.wiley.com/doi/abs/10.1029/JC083iC09p04567 (_eprint: https://onlinelibrary.wiley.com/doi/pdf/10.1029/JC083iC09p04567) doi: 10.1029/JC083iC09p04567

Kolås, E. (2022). *Physical oceanography data from gliders in the Barents Sea, August 2019 - February 2021.* University of Bergen. Retrieved 2022-10-11, from http://metadata.nmdc.no/metadata-api/landingpage/2d5806e47735a4eba2f4c8ead6d03570 doi: 10.21335/NMDC-381060465

Kolås, E. H., Koenig, Z., Fer, I., Nilsen, F., & Marnela, M. (2020). Structure and Transport of Atlantic Water North of Svalbard From Observations in Summer and Fall 2018. *Journal of Geophysical Research: Oceans*, *125*(9), e2020JC016174. Retrieved 2022-12-21, from https://onlinelibrary.wiley.com/doi/abs/10.1029/2020JC016174 (_eprint: https://onlinelibrary.wiley.com/doi/pdf/10.1029/2020JC016174) doi: 10.1029/2020JC016174

Li, S., & McClimans, T. A. (1998, May). The effects of winds over a barotropic retrograde slope current. *Continental Shelf Research*, *18*(5), 457–485. Retrieved 2022-08-23, from https://www.sciencedirect.com/science/article/pii/S0278434397000770 doi: 10.1016/S0278-4343(97)00077-0

Lien, V. S., Schlichtholz, P., Skagseth, Ø., & Vikebø, F. B. (2017, January). Wind-Driven Atlantic Water Flow as a Direct Mode for Reduced Barents Sea Ice Cover. *Journal of Climate*, *30*(2), 803–812. Retrieved 2022-06-22, from https://journals.ametsoc.org/view/journals/clim/30/2/jcli-d-16-0025.1.xml (Publisher: American Meteorological Society Sec-

tion: Journal of Climate) doi: 10.1175/JCLI-D-16-0025.1

Lind, S., Ingvaldsen, R. B., & Furevik, T. (2018, July). Arctic warming hotspot in the northern Barents Sea linked to declining sea-ice import. *Nature Climate Change*, *8*(7), 634–639. Retrieved 2020-02-24, from http://www.nature.com/articles/s41558-018-0205-y doi: 10.1038/s41558-018-0205-y

Loeng, H. (1991, January). Features of the physical oceanographic conditions of the Barents Sea. *Polar Research*, *10*(1), 5–18. Retrieved 2022-08-23, from https://polarresearch.net/index.php/polar/article/view/2294 (Number: 1) doi: 10.3402/polar.v10i1.6723

Loeng, H., Ozhigin, V., & Ådlandsvik, B. (1997, June). Water fluxes through the Barents Sea. *ICES Journal of Marine Science*, *54*(3), 310–317. Retrieved 2023-03-29, from https://doi.org/10.1006/jmsc.1996.0165 doi: 10.1006/jmsc.1996.0165

Lundesgaard, Ø., Sundfjord, A., Lind, S., Nilsen, F., & Renner, A. H. H. (2022, September). Import of Atlantic Water and sea ice controls the ocean environment in the northern Barents Sea. *Ocean Science*, *18*(5), 1389–1418. Retrieved 2023-06-26, from https://os.copernicus.org/articles/18/1389/2022/ (Publisher: Copernicus GmbH) doi: 10.5194/os-18-1389-2022

McDougall, T. J., & Barker, P. M. (2011). *Getting started with TEOS-10 and the Gibbs Seawater (GSW) Oceanographic Toolbox.* SCOR/IAPSO WG127, 28 pp.

Mohamed, B., Nilsen, F., & Skogseth, R. (2022, January). Interannual and Decadal Variability of Sea Surface Temperature and Sea Ice Concentration in the Barents Sea. *Remote Sensing*, *14*(17), 4413. doi: 10.3390/rs14174413

Nilsen, F., Fer, I., Baumann, T. M., Breivik, Ø., Czyz, C., Frank, L., ... Rabault, J. (2021, November). PC-2 Winter Process Cruise (WPC): Cruise Report. *The Nansen Legacy Report Series*(26). Retrieved 2022-09-07, from https://septentrio.uit.no/index.php/nansenlegacy/article/view/6324 (Number: 26) doi: 10.7557/nlrs.6324

Onarheim, I. H., Smedsrud, L. H., Ingvaldsen, R. B., & Nilsen, F. (2014). Loss of sea ice during winter north of Svalbard. *Tellus A: Dynamic Meteorology and Oceanography*, *66*(1), 23933–23941. doi: 10.3402/tellusa.v66.23933

Onarheim, I. H., & Årthun, M. (2017). Toward an ice-free Barents Sea. *Geophysical Research Letters*, *44*(16), 8387–8395. Retrieved 2022-08-17, from https://onlinelibrary.wiley.com/doi/abs/10.1002/2017GL074304 (_eprint: https://onlinelibrary.wiley.com/doi/pdf/10.1002/2017GL074304) doi: 10.1002/2017GL074304

Orvik, K. A. (2022). Long-Term Moored Current and Temperature Measurements of the Atlantic Inflow Into the Nordic Seas in the Norwegian Atlantic Current; 1995–2020. *Geophysical Research Letters*, *49*(3), e2021GL096427. Retrieved 2022-08-18, from https://onlinelibrary.wiley.com/doi/abs/10.1029/2021GL096427 (_eprint: https://onlinelibrary.wiley.com/doi/pdf/10.1029/2021GL096427) doi: 10.1029/2021GL096427

Oziel, L., Sirven, J., & Gascard, J.-C. (2016, January). The Barents Sea frontal zones and water masses variability (1980–2011). *Ocean Science*, *12*(1), 169–184. doi: 10.5194/os-12-169-2016

Padman, L., & Erofeeva, S. (2004). A barotropic inverse tidal model for the Arctic Ocean. *Geophysical Research Letters*, *31*(2). doi: 10.1029/2003gl019003

Parsons, A. R., Bourke, R. H., Muench, R. D., Chiu, C.-S., Lynch, J. F., Miller, J. H., ... Pawlowicz, R. (1996). The Barents Sea Polar Front in summer. *Journal of Geophysical Research: Oceans*, *101*(C6), 14201–14221. Retrieved 2022-08-18, from https://onlinelibrary.wiley.com/doi/abs/10.1029/96JC00119 (_eprint: https://onlinelibrary.wiley.com/doi/pdf/10.1029/96JC00119) doi: 10.1029/96JC00119

Reigstad, M., Wassmann, P., Wexels Riser, C., Øygarden, S., & Rey, F. (2002, December). Variations in hydrography, nutrients and chlorophyll a in the marginal ice-zone and the central Barents Sea. *Journal of Marine Systems*, *38*(1), 9–29. Retrieved 2022-08-17, from https://www.sciencedirect.com/science/article/pii/S0924796302001677 doi: 10.1016/S0924-7963(02)00167-7

Rudels, B., Björk, G., Nilsson, J., Winsor, P., Lake, I., & Nohr, C. (2005). The interaction between waters from the Arctic Ocean and the Nordic Seas north of Fram Strait and along the East Greenland Current: results from the Arctic Ocean-02 Oden expedition. *Journal of Marine Systems*, *55*(1-2), 1–30. doi: 10.1016/j.jmarsys.2004.06.008

Seager, R., Battisti, D. S., Yin, J., Gordon, N., Naik, N., Clement, A. C., & Cane, M. A. (2002). Is the Gulf Stream responsible for Europe's mild winters? *Quarterly Journal of the Royal Meteorological Society*, *128*(586), 2563–2586. Retrieved 2022-08-17, from https://onlinelibrary.wiley.com/doi/abs/10.1256/qj.01.128 (_eprint: https://onlinelibrary.wiley.com/doi/pdf/10.1256/qj.01.128) doi: 10.1256/qj.01.128

Seaglider Quality Control Manual (Version 1.11 ed.). (2012). School of Oceanography and Applied Physics Laboratory University of Washington.

Skagseth, Ø. (2008). Recirculation of Atlantic Water in the western Barents Sea. *Geophysical Research Letters*, *35*(11). Retrieved 2022-08-23, from https://onlinelibrary.wiley.com/doi/abs/10.1029/2008GL033785 (_eprint: https://onlinelibrary.wiley.com/doi/pdf/10.1029/2008GL033785) doi: 10.1029/2008GL033785

Skagseth, Ø., Eldevik, T., Årthun, M., Asbjørnsen, H., Lien, V. S., & Smedsrud, L. H. (2020, July). Reduced efficiency of the Barents Sea cooling machine. *Nature Climate Change*, *10*(7), 661–666. Retrieved 2022-06-22, from https://www.nature.com/articles/s41558-020-0772-6 (Number: 7 Publisher: Nature Publishing Group) doi: 10.1038/s41558-020-0772-6

Skagseth, Ø., Furevik, T., Ingvaldsen, R., Loeng, H., Mork, K. A., Orvik, K. A., & Ozhigin, V. (2008). Volume and Heat Transports to the Arctic Ocean Via the Norwegian and Barents Seas. In R. R. Dickson, J. Meincke, & P. Rhines (Eds.), *Arctic–Subarctic Ocean Fluxes: Defining the Role of the Northern Seas in Climate* (pp. 45–64). Dordrecht: Springer Netherlands. Retrieved 2023-03-30, from https://doi.org/10.1007/978-1-4020-6774-7_3 doi: 10.1007/978-1-4020-6774-7_3

Skogseth, R., Ellingsen, P., Berge, J., Cottier, F., Falk-Petersen, S., Ivanov, B., ... Vader, A. (2019). *UNIS hydrographic database*. Norwegian Polar Institute. Retrieved from https://doi.org/10.21334/unis-hydrography doi: 10.21334/unis-hydrography

Smedsrud, L. H., Ingvaldsen, R., Nilsen, J. E. Ø., & Skagseth, Ø. (2010, February). Heat in the Barents Sea: transport, storage, and surface fluxes. *Ocean Science*, *6*(1), 219–234. Retrieved 2022-10-26, from https://os.copernicus.org/articles/6/219/2010/ (Publisher: Copernicus GmbH) doi: 10.5194/os-6-219-2010

Sundfjord, A., Assmann, K. M., Lundesgaard, Ø., Renner, A. H. H., Lind, S., & Ingvaldsen, R. B. (2020, December). Suggested water mass definitions for the central and northern Barents Sea, and the adjacent Nansen Basin: Workshop Report. *The Nansen Legacy Report Series*(8). Retrieved 2023-02-17, from https://septentrio.uit.no/index.php/nansenlegacy/article/view/5707 (Number: 8) doi: 10.7557/nlrs.5707

Timmermans, M.-L., & Marshall, J. (2020). Understanding Arctic Ocean Circulation: A Review of Ocean Dynamics in a Changing Climate. *Journal of Geophysical Research: Oceans*, *125*(4), e2018JC014378. doi: 10.1029/

2018JC014378

Troupin, C., Beltran, J. P., Heslop, E., Torner, M., Garau, B., Allen, J., ... Tintoré, J. (2015, September). A toolbox for glider data processing and management. *Methods in Oceanography*, *13-14*, 13–23. doi: 10.1016/j.mio.2016.01.001

Visbeck, M. (2002). Deep Velocity Profiling Using Lowered Acoustic Doppler Current Profilers: Bottom Track and Inverse Solutions. *Journal of Atmospheric and Oceanic Technology*, *19*(5), 794–807. doi: 10.1175/1520-0426(2002)019⟨0794:dvpula⟩2.0.co;2

Våge, S., Basedow, S. L., Tande, K. S., & Zhou, M. (2014, February). Physical structure of the Barents Sea Polar Front near Storbanken in August 2007. *Journal of Marine Systems*, *130*, 256–262. Retrieved 2022-08-12, from `https://www.sciencedirect.com/science/article/pii/S0924796311002867` doi: 10.1016/j.jmarsys.2011.11.019

Årthun, M., Eldevik, T., Smedsrud, L. H., Skagseth, Ø., & Ingvaldsen, R. B. (2012, July). Quantifying the Influence of Atlantic Heat on Barents Sea Ice Variability and Retreat. *Journal of Climate*, *25*(13), 4736–4743. Retrieved 2022-08-17, from `https://journals.ametsoc.org/view/journals/clim/25/13/jcli-d-11-00466.1.xml` (Publisher: American Meteorological Society Section: Journal of Climate) doi: 10.1175/JCLI-D-11-00466.1

Årthun, M., Ingvaldsen, R., Smedsrud, L., & Schrum, C. (2011, August). Dense water formation and circulation in the Barents Sea. *Deep Sea Research Part I: Oceanographic Research Papers*, *58*(8), 801–817. Retrieved 2020-02-24, from `https://linkinghub.elsevier.com/retrieve/pii/S096706371100104X` doi: 10.1016/j.dsr.2011.06.001